mater.scichina.com link.springer.com

Published online 18 January 2022 | https://doi.org/10.1007/s40843-021-1906-5
Sci China Mater 2022, 65(4): 855–875

Tunable engineering of photo- and electro-induced carrier dynamics in perovskite photoelectronic devices

Feng Zhang[1†], Zhou Mi[2†], Weizhong Hao[2], Hualong Chen[1], Yule Zhang[1], Jinjin Zhao[2*], Guozhong Cao[3*] and Han Zhang[1*]

ABSTRACT **The last decade has witnessed great progress in photovoltaic technology based on organometal halide perovskites because of their low nonradiative recombination loss, long carrier lifetime, and long diffusion length. The excellent optical properties and easy preparation of organometal halide perovskite-based photovoltaic products enable their wide applications in electro-optical and opto-electrical conversions. In this review, photoinduced free carriers, exciton recombination, and diffusion properties of perovskite photoelectronic devices are discussed. By controlling grain sizes and grain boundaries, suppressing defects, and conducting interfacial charge transfer, their dynamics can be controlled in a versatile manner. The generality and differences in "effective carriers" for device applications, including their electro-optical and opto-electrical conversions, are discussed. In all-optical devices, a strong light-matter interaction causes nonlinear effects, such as two-photon absorption, self-phase modulation, and optical blenching, which enable high-resolution imaging, optical modulation, and optical switching. This review provides a basis for constructing high-performance photoelectronic devices.**

Keywords: perovskites, carrier, exciton, dynamics, photoelectronic devices

INTRODUCTION

Solar cells incorporating organic-inorganic hybrid perovskites (OIHPs) have emerged as the devices with important applications among leading photovoltaic (PV) technologies. The power conversion efficiency (PCE) has increased from 3.8% [1] to over 25.2% for a single planar structure and 28.0% for a tandem structure [2]. All-inorganic thermodynamic perovskite solar cells have reached new record of more than 18% in $CsPbI_3$ [3]. In addition to PV devices, applications based on hybrid perovskites have been widely extended to bright light-emitting diodes (LEDs), nanolasers, photodetectors (PDs), and all-optical devices. Rapid progress and great successes in PVs and LEDs are mainly attributed to the unique combination characteristics of OIHPs, including the following: (1) large absorption coefficient (10^4–10^5 cm^{-1}) and sharp direct-bandgap absorption [4], which enable effective light harvesting with only hundreds of nanometers of film thickness, (2) long carrier lifetime and diffusion length [5,6], (3) a small proportion of nonradiative recombination, indicating the low thermal loss and effective opto-electrical or optical to optical conversions [7], and (4) a desirable and tunable bandgap [8]. For PV and PD devices, effective photocurrent harvesting through the transport layer and minimal loss at the interface is also essential [9,10]. A strong light-matter interaction in low-dimensional perovskites enables a complex nonlinear effect, such as harmonic generation, two-photon absorption, and self-phase modulation, which implies their promising applications in optical switches, modulators, and multiphoton imaging. Multifunctional applications in various photoelectronic devices demand different carrier dynamics. With a complex crystal structure, carrier dynamics can be customized in a versatile manner *via* chemical doping, phase transition, and surface passivation. In the heterojunctions combined with electron/hole transport layers (ETL/HTL) or other semiconductors, charge transfer between layers facilitates carrier transport and increases the harvesting of solar energy.

Numerous excellent review papers have described various aspects of organic-inorganic halide perovskites and their device applications, for example, the fabrication of perovskite thin films toward commercialized solar cells [11]. Photophysical properties [12,13], especially carrier recombination and transport properties [5,14–17], have been investigated by spectroscopic techniques [18–20]. Device applications in solar cells have also been summarized in previous reviews [21,22]. Applications of perovskites have been extended to electro-optical conversion (LEDs and nanolasers), opto-electrical conversion (solar cells and PDs), and all-optical conversion (multiphoton imaging, saturable absorbers (SAs), and optical modulators); however, the common and distinguishing characteristics of photoinduced carrier dynamics and their role have not yet been clarified.

In this paper, we review the fundamental photoinduced species (carriers and excitons) and related dynamic properties in perovskites. These properties can be easily controlled through various strategies, including examining a pristine film in terms of chemical compounds and stoichiometric ratios, microstructures (grain boundary (GB), grain size (GS), and defects), surface passivation, and interfacial charge transfer. The roles of

[1] Collaborative Innovation Center for Optoelectronic Science and Technology International Collaborative Laboratory of 2D Materials for Optoelectronics Science and Technology of Ministry of Education Institute of Microscale Optoelectronics, Shenzhen University, Shenzhen 518060, China
[2] School of Materials Science and Engineering, Shijiazhuang Tiedao University, Shijiazhuang 050043, China
[3] Department of Materials Science and Engineering, University of Washington, Seattle, WA, 98195-2120, USA
[†] These authors contributed equally to this work.
[*] Corresponding authors (emails: jinjinzhao2012@163.com (Zhao J); gzcao@u.washington.edu (Cao G); hzhang@szu.edu.cn (Zhang H))

an "effective carrier" in various optoelectronic devices, including solar cells, LEDs, optical switches, and PDs, are discussed (Fig. 1). This review will help elucidate the mechanism of "effective carriers" in these devices and provide a basis for designing high-performance optoelectronic devices.

FUNDAMENTAL OF PEROVSKITES

Crystal structure

Hybrid/all-inorganic perovskites comprise compounds with an ABX_3 crystal structure (Fig. 2a), which refers to the mineral $CaTiO_3$, where A is a large organic cation (e.g., methylammonium = MA^+ ($CH_3NH_3^+$), butylammonium = BA^+ ($C_4H_9NH_3^+$), formamidinium = FA^+ ($NH_2CH{=}NH_2^+$), and phenylethylammonium = PEA^+ ($C_6H_5(CH_2)_2NH_3^+$)) or an inorganic cation (e.g., Cs^+ and Rb^+) [3,21]. B is a divalent element, such as Pb^{2+}, Ge^{2+}, Sn^{2+}, Cu^{2+}, Mn^{2+}, Zn^{2+}, Cr^{2+}, and Cd^{2+}, and X is a halogen, such as I^-, Br^-, and Cl^- [13]. Furthermore, mixed organic cations (MA^+/FA^+) or triple-cation approaches ($MA^+/FA^+/Cs^+$) [22], mixed metal cations (Sn^{2+}/Pb^{2+}) [5], and mixed halides (Br^-/I^-) have been developed [10,23,24]. In bulk perovskites, anion X^- together with B^{2+}, form the framework of corner-sharing BX_6 octahedra and B^{2+} usually forms a specific crystal structure that is easily affected by material dimensions, temperature, and pressure [25,26].

In addition to perovskites with a three-dimensional (3D) morphology, low-dimensional perovskites, i.e., 2D nanoplates [27,28], 1D nanowires [29,30], and 0D quantum dots (QDs) [31,32], have been developed [31,33–35]. Low-dimensional perovskites possess unique photophysical properties to retain the electron behavior in a limited region. As a result, size-related quantum confinement should occur if the size of materials is comparable to the de Broglie wavelength of the electron wavefunction, thus modifying the energy levels. In comparison with van der Waals 2D nanomaterials, such as graphene, black phosphorus (BP), and transition-metal dichalcogenides (TMDCs), the connection between layers in low-dimensional perovskites is ionic in nature (ionic bonding). In contrast to the 3D morphology with an ABX_3 structure, 2D Ruddlesden-Popper perovskites (RPPs) have the following formula: $(LA)_2A_{n-1}B_nX_{3n+1}$, where LA or A is a Group IA monovalent cation or a monovalent organic molecule cation, B is a divalent Group IVA cation, X is a halogen anion and n indicates the number of the metal cation layers between the two layers of the organic chains [36]. Fig. 2b shows the structure of RPPs (n =1, 2, and 3) and the corresponding bulk counterpart (n =∞). When $n \rightarrow \infty$, the 2D RPP phase transforms to a 3D structure similar to $BaTiO_3$. Thus far, many combinations, including $(BA)_2(MA)_{n-1}Pb_nI_{3n+1}$ [28,37], $(PEA)_2(MA)_{n-1}Pb_nI_{3n+1}$ [38,39], $(BA)_2(MA)_{n-1}Sn_nI_{3n+1}$ [38], $Cs_{n+1}Pb_nI_{3n+1}$ [39], and $(BA)_2PbBr_4$ [27], have been proposed. Yang *et al.* [40] systematically studied the structural stabilities of 2D halide perovskites. These perovskites normally possess an orthorhombic or tetragonal struc-

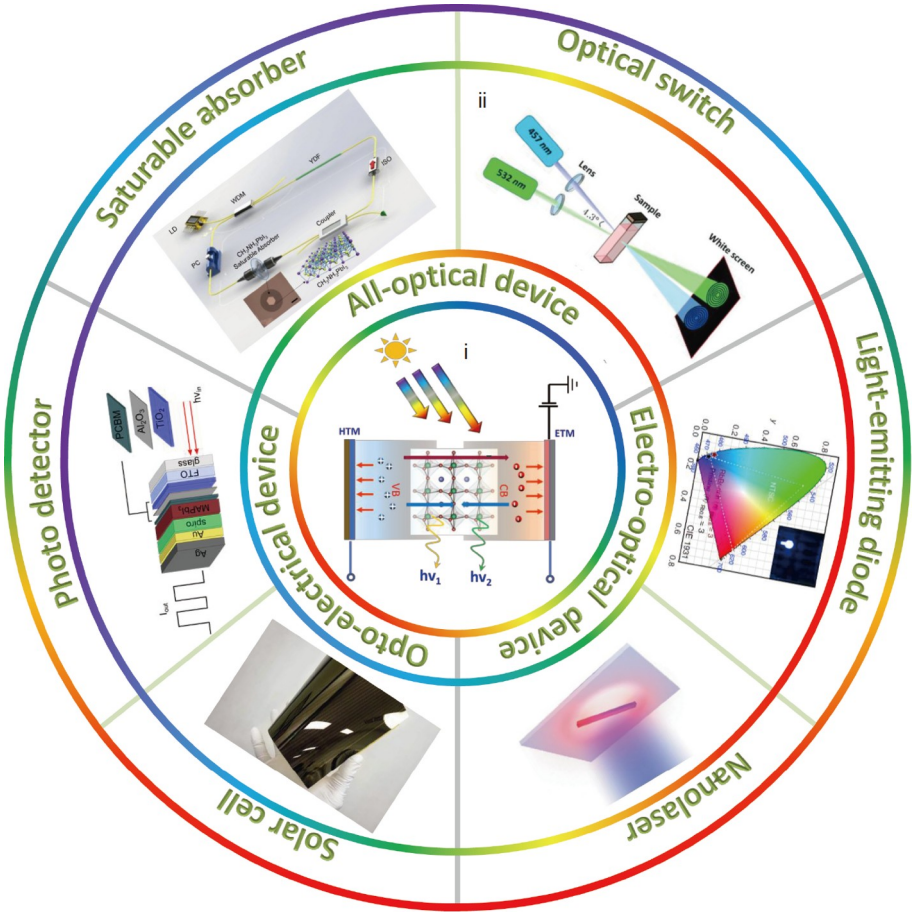

Figure 1 Roadmap of this review. (i) Carrier generation, recombination, and diffusion dynamics. (ii) Device applications, including electro-optical, opto-electrical, and all-optical devices.

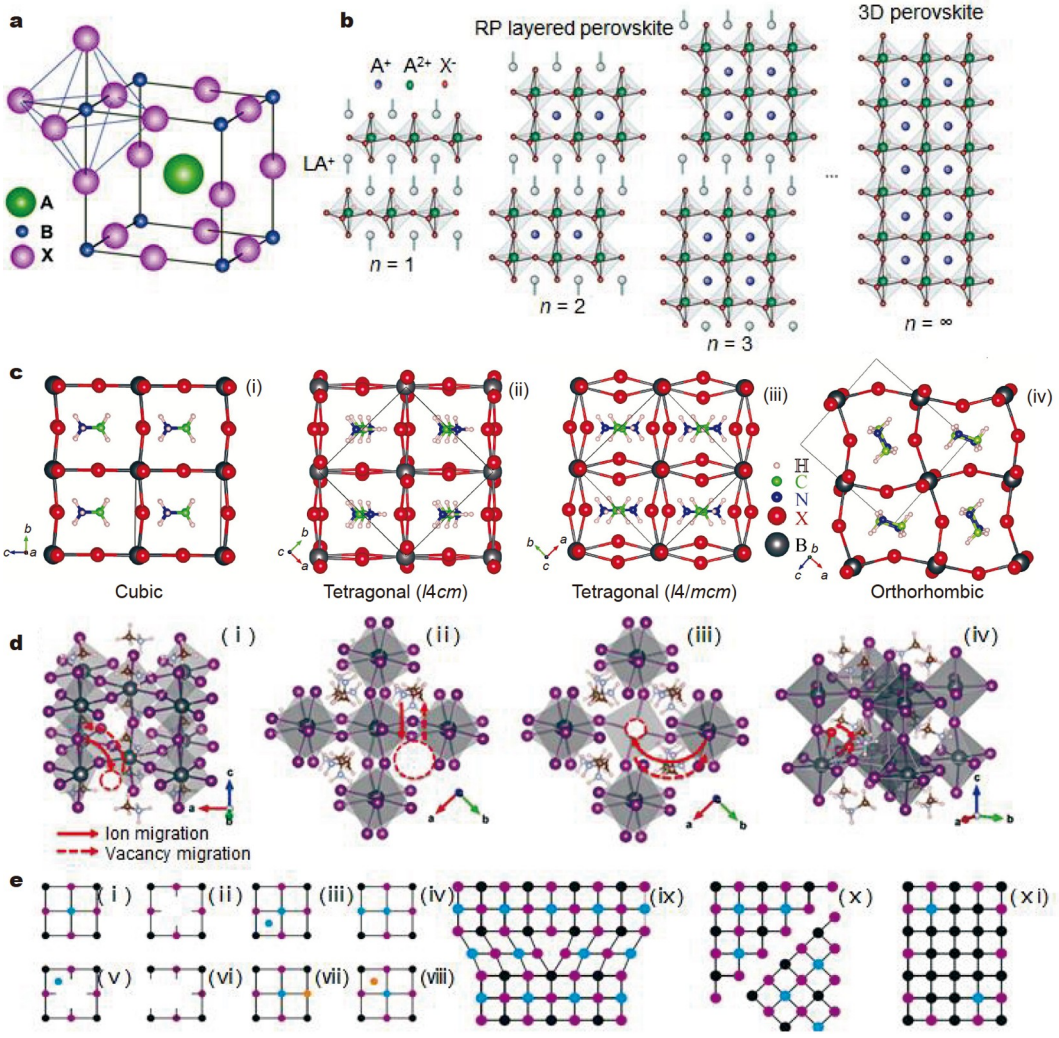

Figure 2 Crystal structure of hybrid perovskite. (a) Typical perovskite structure with the ABX_3 formula, where A, B, and X indicate a large organic cation, a divalent element, and a halogen, respectively. Reprinted with permission from Ref. [45]. Copyright 2015, Elsevier. (b) 2D-layered perovskites with $(LA)_2A_{n-1}B_nX_{3n+1}$ (n = 1, 2, and 3) formula and 3D morphology when $n = \infty$. LA is a Group IA monovalent cation or a monovalent organic molecule cation. A, B, X, and LA are represented by a blue circle, a green circle, an orange circle, and a gray circle, respectively. Reprinted with permission from Ref. [46]. Copyright 2019, Springer Nature. (c) Representation of the crystal structures of cubic, tetragonal (space group: *I*4*cm*), tetragonal (*I*4/*mcm*), and orthorhombic perovskites. Reprinted with permission from Ref. [47]. Copyright 2018, OP Publishing Ltd. (d) (i) V_I, (ii) V_{MA}, (iii) V_{Pb}, and (iv) I_i defect diffusion paths. Vacancies are highlighted with dashed circles. Brown = C, white = H, purple = I, blue = N, and black = Pb atoms. Reprinted with permission from Ref. [48]. Copyright 2015, Royal Society of Chemistry. (e) Defects in a perovskite crystal lattice (black, blue, and purple dots represent M^-, A^-, and site ions, respectively): (i) perfect lattice, (ii) vacancy, (iii) interstitial, (iv) antisite substitution, (v) Frenkel defect, (vi) Schottky defect, (vii) substitutional impurity, (viii) interstitial impurity, (ix) edge dislocation, (x) GB, and (xi) precipitate. Reprinted with permission from Ref. [49]. Copyright 2016, Springer Nature.

ture and exhibit more flexibility and deformability than their bulk morphology. Moreover, their structure is easily affected by the external pressure [41] because the alignment of Pb–I–Pb bond angles cause a phase transition (a tetragonal phase to a cubic phase) above 0.3 GPa [42]. The space group changes from $Pm\bar{3}m$ to $Im\bar{3}$ in $MAPbBr_3$ and from $Fmmm$ to $Im\bar{3}$ in $MAPbI_3$ [43]. Wang *et al.* [44] found a similar result, i.e., the space group changes from $Pm\bar{3}m$ to $Im\bar{3}$ and then to $Pnma$ in $MAPbBr_3$. The phase structure of $MAPbBr_3$ is sensitive to temperature but not to pressure. Fig. 2c illustrates the space groups of perovskites.

Ions (MA^+ and I^-) and defects in perovskites diffuse when an electric field is applied (Fig. 2d), causing unconventional photocurrent hysteresis in perovskite-based solar cells. Defects are inevitable species in the solution-processed perovskites, which considerably affect the electronic band structures, carrier dynamics, and related device performance. Defects in perovskites can be categorized, as shown in Fig. 2e. Perovskite thin films are mostly fabricated by simply spin/drop coating the films with a colloidal solution. Unintentional defects inevitably form and yield trap states and recombination centers. The high PCE of solar cells suggests that hybrid perovskites have a high tolerance for defect-related potential losses. Thus far, the highest PCE is lower than the thermodynamic limit of ~30%–33% for bandgaps of perovskites in the range of 1.2–1.6 eV [50]. Defects remain one of the most crucial crystal characteristics that hinder further progress for increasing PCE and obtaining stable solar cells [49].

Optical absorption, emission, and electronic band structure

PV and LED devices have high performances because of their

unique optical absorption and emission characters. The $MAPbI_3$ perovskite has a large absorption coefficient of up to 10^4–10^5 cm^{-14}; consequently, a large amount of solar energy is harvested in a solution-processed film that is as thin as hundreds of nanometers. Tunable optical absorption and emission bands are quite attractive in stack-structure solar cells and full-band LEDs. The optimal bandgap of single-junction solar cells is designed to be 1.1–1.4 eV to harvest the photon energy of solar irradiation effectively, whereas the most popular perovskite, namely, $MAPbI_3$, has a relatively large bandgap of ~1.55 eV, restraining the effective harvesting of energy above the bandgap [51]. Thus, the absorption band should be tuned, for example, by dimension tailoring and chemical compound controlling, as presented in Fig. 3a, b.

The ground state transition of $MAPbI_3$ perovskite at R and M point is presented in Fig. 3c, corresponding to the two lowest energy transitions $F_{3/2,g} \rightarrow E_{1/2,u}$ and $E_{1/2,g} \rightarrow F_{3/2,u}$ and a series of optically allowed transitions between R and M point. The optical absorption and carrier dynamics have been investigated by transient absorption spectroscopy [52]. The bandgap is determined by the energy difference between the upper VBM_2 and the CBM. This transition is correlated with the fundamental electronic band structure. In Pb-halide perovskites, the VBM comprises antibonding states, which are derived from the hybridizations of the atomic 5p orbitals of I and 6s orbitals of Pb; conversely, the CBM mainly comprises empty 6p orbitals of Pb (Fig. 3e). The split band of the valence and conduction bands yields a wide continuum absorption from the absorption onset, where electrons transit vertically and instantly *via* the Franck-Condon principle [53]. After being photoexcited to a high-energy state, the free charges or excitons achieve intraband equilibrium and recombine radiatively or nonradiatively. Most hybrid metal perovskites possess a direct band structure and a moderate band gap, covering most of the solar radiation spectra. The first-principle calculation indicates that a hybrid $MAPbI_3$ perovskite possesses a direct bandgap of 1.51–1.63 eV [54]. In bulk perovskites, the electronic bandgap is close to the optical bandgap for the small exciton binding energy of tens of millielectronvolt [55]. Although large organic MA^+ can effectively stabilize crystal structures, it does not affect the electronic structure at the band edge. The occupied s orbital of Pb^{2+} has a strong antibonding coupling with p orbital of I; thus, upper valence bands become dispersive [56].

The bandgap structure and value of semiconductor per-

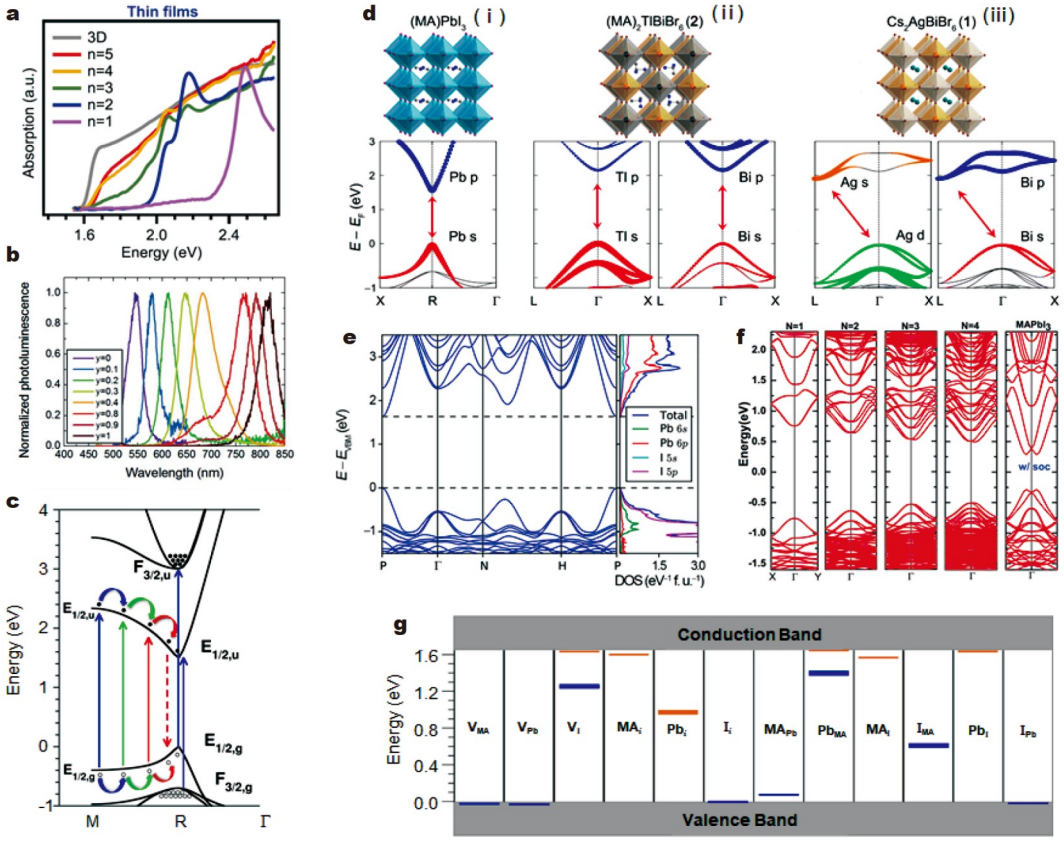

Figure 3 Optical absorption, emission, and electronic band structure alignment. (a) Absorption of thin films *versus* n in the $(BA)_2(MA)_{n-1}Pb_nI_{3n+1}$ perovskite. Reprinted with permission from Ref. [57]. Copyright 2017, American Association for the Advancement of Science. (b) Emission of $FAPbI_yBr_{3-y}$ perovskites with varying y. Reprinted with permission from Ref. [58]. Copyright 2014, Royal Society of Chemistry. (c) Schematic of the band structure of the cubic perovskite phase of $MAPbI_3$, including spin-orbit coupling through which the colorful arrows show optical absorption and emission. Reprinted with permission from Ref. [59]. Copyright 2014, American Chemical Society. (d) Crystal and band structures of (i) $(MA)PbI_3$, (ii) $(MA)_2TlBiBr_6$, and (iii) $Cs_2AgBiBr_6$. Reprinted with permission from Ref. [60]. Copyright 2017, American Chemical Society. (e) Band structure and density of states of $MAPbI_3$ when the pressure is P = 1.8 GPa. Reprinted with permission from Ref. [43]. Copyright 2016, American Chemical Society. (f) Calculated band structures *versus* the layer thickness of the $(PEA)_2PbI_4$ (n = 1–4) perovskite. Reprinted with permission from Ref. [39]. Copyright 2017, American Chemical Society. (g) Trap-state levels of 12 intrinsic defects in the $MAPbI_3$ perovskite. Reprinted with permission from Ref. [61]. Copyright 2014, American Chemical Society.

ovskites can be tailored in a versatile manner by selecting different metal cations [62], inorganic anions [1], and organic ligands [63]. The bandgap increases as the size of the cation decreases. At the M site, changing the cation from Pb^{2+} to the less toxic Sn^{2+} forms $MASnI_3$ and shifts the bandgap from 1.55 to 1.3 eV. Replacing the MA^+ with a slightly larger FA^+ results in the bandgap shifting from 1.57 to 1.48 eV; when MA^+ is replaced with a smaller cesium ion, the bandgap changes to 1.73 eV [58]. The double perovskite $(MA)_2TlBiBr_6$, where Pb^{2+} is replaced with isoelectronic Bi^{3+} and Tl^+, has a similar orbital composition at its band edge. The inclusion of Ag s (Ag d) orbitals in $(MA)PbI_3$ changes the CBM and the VBM, leading to an indirect gap [60] (Fig. 3d). Friend's group [64] found that the bandgap can be tuned by varying the chloride to bromide ratio in a $MAPb(Br_xCl_{1-x})_3$ ($0 \leq x \leq 1$) perovskite. As the chloride fraction increased from 0% to 100%, the bandgap increased from 2.3 to 3.1 eV. Snaith's group [65] investigated the absorption band-edge shifts in mixed anions and cations for obtaining optimal solar cells, where the absorption wavelength onset decreased as the Br fraction increased in $FAPb[I_{(1-x)}Br_x]_3$ and $FA_{0.83}Cs_{0.17}Pb[I_{(1-x)}Br_x]_3$.

The bandgap is sensitive to the thickness of a layered perovskite because of the quantum confinement effect. In the layered $(BA)_2(MA)_{n-1}Pb_nI_{3n+1}$ perovskite, the optical bandgap monotonously increases from 1.85 to 2.42 eV when n decreases from 5 to 1 [57]. Experimental observations [66] reveal that the calculated band structures of $(PEA)_2PbI_4(n)$ and $Cs_2PbI_4(n)$ based on density functional theory show a decrease in their bandgaps as the layer thickness (n) increases [39] (Fig. 3f). Further, the optical bandgaps of hybrid halide perovskite materials can be tuned by the pressure [26,42–44]. In an $MAPbI_3$ perovskite, the bandgap undergoes a noticeable shift from 1.537 eV at 0.1 GPa to 1.507 eV at 0.32 GPa. When the pressure increases up to 2.1 GPa, the bandgap is optimized to obtain the desired single-junction solar cells in Pb-based perovskites [67]. Solution-processed perovskite films have a non-negligible defect concentration, as presented in Fig. 2e. These defects generate deep or shadow trap states (Fig. 3g) and eventually affect the carrier dynamics.

Free carrier and exciton

Excitons, the bound state of an electron-hole pair generated *via* Coulomb interaction, and the free carrier are the fundamental photoinduced species in perovskites. Fig. 4a shows the intraband free carrier and exciton contribution to the total absorption spectrum of $MAPbI_3$. The ease of exciton dissociation is quite essential to effectively harvest the photocurrent in solar cells and PDs. In thermodynamic equilibrium, the fraction of free carriers and exciton (x) is determined using the exciton binding energy (E_b) and excitation density (n_c). Under the PV working regime (n_c is ~10^{13}–10^{15} cm^{-3}), the exciton-exciton interaction is neglected, which occurs at a high density of >10^{20} cm^{-3}. The fraction of the free carrier and exciton can be depicted by the

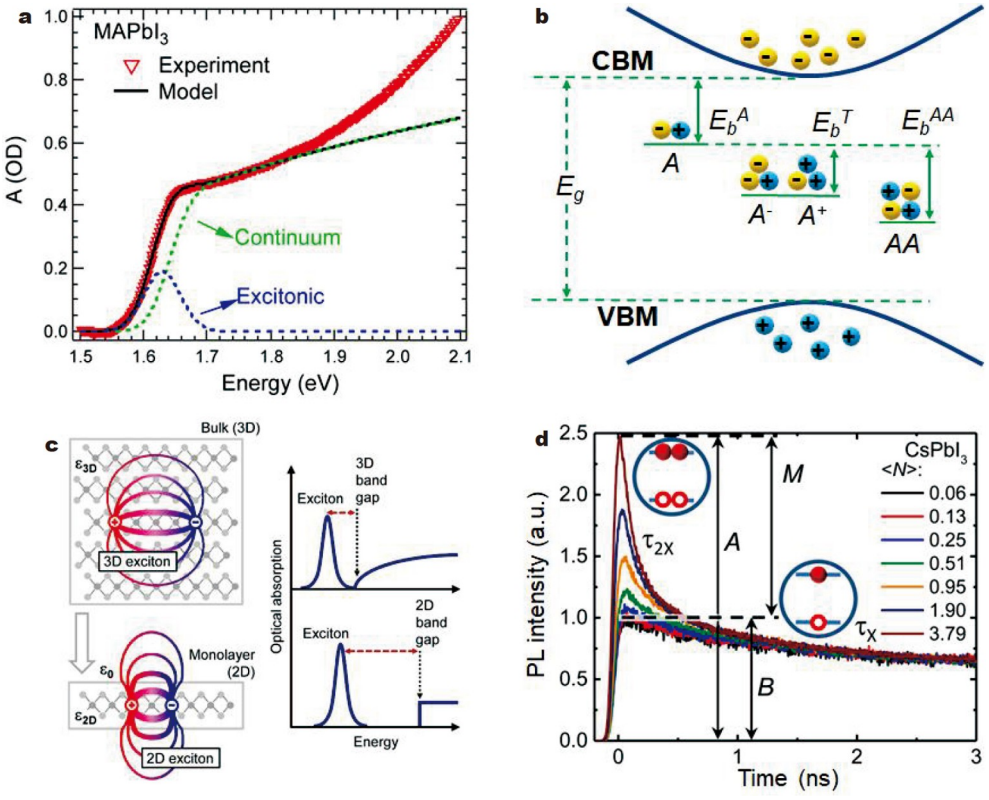

Figure 4 (a) Contribution of continuum and exciton to the total optical absorption. Reprinted with permission from Ref. [76]. Copyright 2016, Springer Nature. (b) Schematic of the free carrier, exciton, trion, biexciton, and the corresponding exciton binding energy. (c) Representation of electrons and holes bound to excitons for the bulk and monolayer semiconductor. Reprinted with permission from Ref. [77]. Copyright 2014, American Physical Society. (d) TRPL traces *versus* the pump fluence of $CsPbI_3$ QDs. The multiexciton signal is represented by $M = A - B$. M, A and B are amplitude of the multiexciton signal, the amplitudes of the total PL signal and its single-exciton component. $\langle N \rangle$ is the average number of excitons generated in one QD. Reprinted with permission from Ref. [32]. Copyright 2016, American Chemical Society.

Saha-Langmuir equation, $\frac{x^2}{1-x} = \frac{1}{n_c}\left(\frac{2\pi\mu k_B T}{h^2}\right)^{3/2} e^{-\frac{E_b}{k_B T}}$, applying the law of the mass action of Wannier-Mott excitons [68]. Several investigations on the exciton and exciton binding energy have been reported. D'Innocenzo *et al.* [68] found that free charges are the dominant photoinduced species at room temperature for operating solar cells ($n < 10^{15}$ cm^{-3}). With a decrease in temperature, the proportion of the exciton increases. This finding is partially attributed to the small exciton binding energy of tens of millielectronvolt (~55 meV for the $MAPbI_{3-x}Cl_x$ mixed perovskite [68] and 16 meV for $MAPbI_3$ [55]), which can be experimentally characterized using the diamagnetic shift of magnetoabsorption [69], temperature dependence of photoluminescence (PL) intensity [70–72], analysis of absorption onsets [57,68,73], and excitonic resonances in magnetoabsorption [55]. This exciton binding energy in bulk perovskites is low enough to be depicted by the Wannier-Mott model, through which relatively large dielectronic constants induce a reduced Coulomb interaction. A small exciton binding energy means that excitons can easily dissociate into a free charge at room temperature ($E = k_B T_R = 26$ mV), where k_B is the Boltzmann constant, and T_R is the thermodynamic temperature. The value presents the magnitude of the conventional III–V semiconductor QDs and is smaller than the value of 2D semiconductors, such as BP and TMDCs [74,75].

With quantum confinement and reduced dielectric confinement in low-dimensional perovskites, electrons and holes are strongly bonded *via* Coulombic interaction in the forms of one electron and one hole (exciton), one electron and two holes, two electrons and one hole (trions), and two electrons and two holes (biexciton). Studies have focused on multibody complexes and their spectroscopic signature except for the neutral single exciton. A schematic of their binding energy and the corresponding emission energy is shown in Fig. 4b. In a low-dimension limit, the exciton binding energy is larger than that of the bulk morphology. In 2D-exfoliated RPP crystals, exciton binding energies as a function of n reach 380, 270, and an average value of 220 meV for $n = 1$, $n = 2$, and $3 \leq n \leq 5$, respectively. These values are several times larger than those of a 3D perovskite for quantum confinement and reduced dielectric screening [57], as shown in Fig. 4c. If electrons and holes have opposite spins, two particles can easily recombine and emit photons. These electron-hole pairs are called bright excitons. However, if they have the same rotation, electrons and holes cannot easily recombine. Such excitons cannot emit light; as such, they are called dark excitons. In addition to bright excitons, dark excitons have been found in perovskite nanocrystals (NCs) [78–81]. At a low-temperature stable crystalline phase, where the exciton band continuously exists, the "Varshni" trend causes the blue shift of the absorption band edge. Except for free carriers and excitons, conducting plasma and unbound but Coulomb-correlated electron-hole pair can be photoexcited. Carrier-carrier interactions are considerably enhanced because of the strong quantum confinement in a low-dimensional perovskite; consequently, this phenomenon can prioritize carrier cooling *via* Auger recombination, which is a reversible process of carrier multiplication (CM). Under high photoexcitation, multibody complexes are observed. Makarov *et al.* [32] investigated the spectral and dynamical properties of single excitons and biexcitons in Cs-Pb-halide perovskite QDs. Fluence-dependent PL traces show that a fast decay component increases as the fluence increases. The increasing fast decay signal in time-resolved PL (TRPL) is attributed to biexciton decay, with a time constant of 93 ps for $CsPbI_3$, which is confirmed by the amplitude of the TRPL *versus* the pump fluence. At moderate excitation levels ($\langle N \rangle < 0.5$), the amplitude of M is proportional to the Poisson probability p_2 or $\langle N \rangle^2$; in this case, the dominant multibody species are biexcitons.

In perovskite QDs, slowed-down carrier relaxation facilitates CM, which is known as multiple excitons. This indicates that a single exciton under a high exciton transfers its energy to another exciton and generates multiple electron-hole pairs. This process is the reverse of Auger recombination. de Weerd *et al.* [82] reported efficient CM in the $CsPbI_3$ perovskite NCs. Under a linear excitation regime, namely, the number of absorbed photons per nanocrystal at a very low level ($\langle N_{exc} \rangle << 1$), a fast component rises when the excitation energy surpasses the CM threshold. The CM efficiency reaches 98% when the excitation energy is 2.4 times that of the bandgap (Fig. 4d). This Auger-effect-induced CM helps reduce the energy loss above the bandgap in solar energy collection.

CARRIER DYNAMICS AND TUNABILITY

Recombination and diffusion dynamics

Recombination dynamics

After photoexcitation, electrons are instantly generated in the valence band, thereby leaving holes in the conduction band and forming excitons below the bandgap. The generated carrier density is directly determined in terms of the optical intensity of light [83]. For PV devices working under AM 1.5 solar spectral irradiation, the charge carrier density n_c is low, i.e., 10^{15}–10^{16} cm^{-3}; for perovskite-based lasers, the value is much higher, which is up to 10^{20} cm^{-3}. The charge carrier density is a crucial parameter and considerably affects recombination paths in related devices, such as solar cells, LEDs, PDs, and laser devices. The charge carrier recombination dynamics in hybrid perovskites revealed by time-resolved spectroscopies or transient photocurrent techniques can be understood by probing the charge carrier density in terms of different mechanisms, which can be expressed by the third-order rate equation [15,84]:

$$\frac{dn_c}{dt} = -k_3 n_c^3 - k_2 n_c^2 - k_1 n_c, \quad (1)$$

where n_c is the carrier density, k_1 is the trap-assisted monomolecular recombination rate constant in which "monomolecular" indicates an exciton (i.e., a bound state of electron-holes pair, an electron, or a hole), k_2 is the bimolecular (electron and hole) recombination rate constant, and k_3 is the Auger recombination rate constant. The schematic of recombination is shown in Fig. 5a.

Trap-assisted recombination, also referred to as Shockley-Read-Hall (SRH) recombination, happens when an electron or a hole falls into a "trap" state, which is caused by the presence of foreign atoms or crystal defects. This recombination involves two steps. A free electron that falls into a "trap" state falls into an empty state in the valence band and recombines with the free hole, thereby completing recombination. At low fluences, SRH recombination is the dominant recombination mechanism, which limits the PL efficiency. At high fluences, the trap states

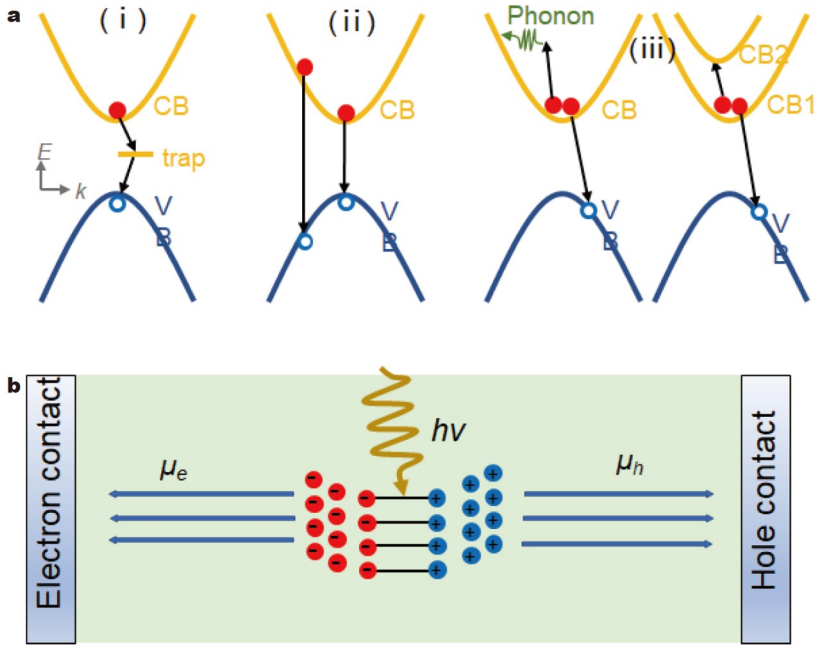

Figure 5 Carrier dynamics in perovskites. (a) Mechanisms of the charge carrier recombination, (i) trap-assisted monomolecular recombination, (ii) bimolecular recombination, and (iii) multibody Auger recombination. (b) Schematic of carrier diffusion in perovskites.

are predominantly filled and the recombination of the photogenerated carriers is dominated by radiative processes [85–87]. The discussion in the previous section has shown that most of the defects with low formation energy yield a shallow energy level and the deep subgap leads to rapid nonradiative recombination. The GS, surface, and GBs should be optimized by controlling the trap state through surface passivation to modulate trap-mediated recombination. Bimolecular recombination, namely, band-to-band recombination, occurs when electrons fall from the conduction band into the empty state of the valence band and recombine with the hole. This band-to-band transition also indicates the radiative transition in direct-bandgap semiconductors. Intensity-dependent recombination follows a simple rate equation, including monomolecular recombination and bimolecular radiative recombination. Therefore, carrier lifetime decreases inversely with excitation intensity when the excitation intensity is above 20 nJ cm^2 [87].

Multibody Auger recombination is not a process by which an electron and a hole can recombine directly, but the carrier releases its energy to another carrier [88,89]. In some instances, an carrier may also interact with phonons. Under high-energy excitation, the generated electron-hole pair releases its energy to another pair, causing multiple exciton generation, that is, CM. In low-dimensional perovskites, the exciton is spatially confined for quantum confinement. Carrier-carrier scattering enhances when energy in continuous energy band (bulk semiconductors) is modified to discrete energy level (QDs), facilitating CM [83]. The interaction of a charge carrier with a phonon sets a fundamental intrinsic limit to carrier mobilities and governs emission line broadening in perovskites. Moreover, it influences carrier cooling above the bandgap excitation. Electron scattering from the longitudinal optical phonon *via* Fröhlich interaction is the dominant process at room temperature, whereas this process from acoustic phonons is negligible [90]. Phonon scattering mechanisms are phonon-impurity scattering, Umklapp phonon-phonon scattering, phonon-boundary scattering, and phonon-electron scattering, which can be characterized *via* the recombination rate ($1/\tau$, the inverse of relaxation time). Yang *et al.* [73] clarified that carrier cooling is slow because of the hot-phonon bottleneck effect. A longitudinal optical phonon model can be used to model carrier cooling in MA Pb-halide perovskite, whose energy loss is dominated by the carrier-phonon interaction:

$$\frac{\mathrm{d}U_c}{\mathrm{d}t} = \frac{3k_B}{2}\frac{\mathrm{d}T_e}{\mathrm{d}t} \approx \hbar\omega_{LO} / \tau_{ave}\left[\exp\left(-\frac{\hbar\omega_{LO}}{k_B T_e}\right) - \exp\left(-\frac{\hbar\omega_{LO}}{k_B T_L}\right)\right], \quad (2)$$

where T_e and T_L are the electron and lattice temperatures, respectively, and τ_{ave} is the time constant characterized by phonon emission, which increases by three orders of magnitude (from ~30 fs to ~30 ps) when the carrier density increases from 5.2×10^{17} to 6.0×10^{18} cm^{-3}. Such slow thermalization at a high carrier density is ascribed to a hot-phonon bottleneck, which occurs in a nonequilibrium phonon population with a high phonon emission rate under high n_0. Price *et al.* [91] observed a similar reduced carrier cooling process at a high fluence at which the decay lifetime changes from 230 to 770 fs when the carrier density increases from 6×10^{17} to 60×10^{17} cm^{-3}.

Recombination dynamics in perovskites can be characterized by time-resolved spectroscopies, including transient absorption spectroscopy (TAS), TRPL, time-resolved terahertz absorption spectroscopy (TRTAS), and time-resolved microwave conductivity (TRMC). TAS and TRPL can directly probe the carrier lifetime at the excited state, and the former can provide broadband information for radiative and nonradiative carrier combinations. By comparison, the latter can only probe radiative dynamics. Previous investigations suggested that radiative bimolecular recombination dominates at high initial carrier densities ($n_0 > 10^{17}$ cm^{-3}) [52,92,93]. At lower excitation densities, such as those under a solar cell working condition, trap-mediated recombination is widely used to clarify the carrier

dynamics by which relaxation shows the following order: single exponential [94,95] to biexponential [96,97] to stretched exponential [98] functions with varying fidelity levels.

Carrier recombination can be exactly determined on the basis of advanced techniques. Herz and co-workers [83] revealed the contribution of the three mechanisms to the total recombination by fitting the transient terahertz transmittance to the third-order recombination equation under the excitation of 6 μJ cm^2 (photon density = 6×10^{17} cm^{-3}); conversely, the first-order constant k_1 can be obtained by fitting the TRPL data to exponential function under a low excitation of 0.03 μJ cm^2, corresponding to a photon density of 10^{15}–10^{16} cm^{-3} based on the above calculations. In the mixed halide perovskite, $MAPbI_{3-x}Cl_x$ should possess a longer carrier lifetime and diffusion than those of triiodide $MAPbI_3$, even under relatively high excitation energy. k_1 of the mixed halide perovskite is smaller (4.5 μs^{-1}), although it is much larger than that of the triiodide ($MAPbI_3$ (3:1) = 15 μs^{-1} and $MAPbI_3$ (1:1) = 14 μs^{-1}). Second-order constants show the same trend ($MAPbI_{3-x}Cl_x$ = 8.7×10^{-11} cm^3 s^{-1}, $MAPbI_3$ (3:1) = 9.4×10^{-10} cm^3 s^{-1}, and $MAPbI_3$ (1:1) = 9.2×10^{-10} cm^3 s^{-1}), whereas the third-order constants have a reverse trend ($MAPbI_{3-x}Cl_x$ = 9.9×10^{-29} cm^6 s^{-1}, $MAPbI_3$ (3:1) = 3.7×10^{-29} cm^6 s^{-1}, $MAPbI_3$ (1:1) = 1.3×10^{-28} cm^6 s^{-1}).

Diffusion dynamics

Carrier transport and diffusion are critical processes in PV and PD devices. Diffusion should be long, especially in a planar heterostructure, which has been widely accepted as the requirement for the high performance of perovskite-based solar cells (Fig. 5b), to effectively harvest the photocurrent. According to the following equation, $L_D = \sqrt{\frac{D}{r(n)}} = \sqrt{\frac{\mu k_B T}{r(n)e}}$, where L_D, D, μ, k_B, and T are the carrier diffusion length, diffusion constant, carrier mobility, Boltzmann constant, and temperature [83], respectively. It is easily deduced that high carrier mobility and a small carrier recombination rate are beneficial to long diffusion. Carrier diffusion properties can be modeled by fitting the TAS or TRPL decay dynamics to the 1D diffusion equation [98,99], which has been applied to understand the exciton/free charge transportation of organic- or perovskite-based solar cells:

$$\frac{\partial n_c(x,t)}{\partial t} = D\frac{\partial^2 n_c(x,t)}{\partial x^2} - k(t)n_c(x,t), \quad (3)$$

where $k(t)$ is the PL decay rate without any electron/hole transporting layers as quenchers. In this scenario, the obtained D is the total carrier diffusion, incorporating an electron and a hole. In a solution-processed perovskite film, a large absorption coefficient of up to 10^4–10^5 cm^{-1} ensures that the thin film with hundreds of nanometers can absorb most of the sunlight.

Peng *et al.* [18] summarized various techniques to monitor the carrier transport properties. The diffusion coefficient can be obtained by fitting the dynamics to the 1D diffusion equation mentioned above. In optical pumped TRTAS and TRMC measurements, the photoinduced carrier density with time evolution is correlated with the changes in terahertz or microwave conductivity ($\Delta\sigma$) and carrier mobility can be deduced from the following equations:

$$\mu = \frac{\Delta\sigma}{\xi n_{exc} e}, \quad (4)$$

$$\frac{\Delta P}{P} = A\Delta\sigma(t) = Ae(\Delta n_e(t)\mu_e + \Delta n_h(t)\mu_h), \quad (5)$$

where ξ is the quantum yield of charge generation, n_{exc} is the excitation density, e is the elementary charge, ΔP is the relative change in the power, n_e and n_h are the populations of the mobile electrons and holes, and μ_e and μ_h are the mobilities of electrons and holes, respectively.

One of the important characters of perovskite is its long diffusion length (L_D) of up to or greater than the thickness of the absorber and absorption depth ($d = 1/\alpha$). However, the determined L_D is sensitive to many factors, such as characterization techniques, sample morphologies, and compositions. L_D of $MAPbI_3$ ranges from ~100 nm [98] to tens of micrometer [6], which is usually longer than the absorption depth of 100–200 nm. This value is much larger than that of the solution-processed and thermally deposited organic molecules [99]. Charge transport can be affected by the layer thickness and ratio of MA^+ to PEA^+; the perovskite with an intermediate PEA^+ content (50%) possesses the longest diffusion length of 2.5 μm, which is longer than that of the bulk $MAPbI_3$ (2.2 μm) and 2D $(PEA)_2PbI_4$ (60 nm) [100]. In the mixed hybrid perovskite $MAPbI_{3-x}Cl_x$ with additive chloride ion, the carrier diffusion can be longer [94,101]. Using impedance spectroscopy measurements, the ambipolar diffusion lengths of the coupled electron-hole transport of $MAPbI_3$ and $MAPbI_{3-x}Cl_x$ are 1000 and 1400 nm, respectively [101]. For low defects and recombination centers, the diffusion length of a single crystal is much longer than that of the polycrystal. With a long carrier lifetime and diffusion length, the PV performance is high [102]. Carrier transport is longer in a planar thin film than that in a mesostructured analog with Al_2O_3 perovskites [16]. As temperature increases, the carrier mobility and diffusion length of $MAPbI_3$ decrease from 3 μm at −93°C to 1.2 μm at 67°C [103], which is closely correlated with temperature-induced phase transition. All-inorganic 11-nm colloidal $CsPbBr_3$ NCs have excellent carrier transport properties of ~4500 cm^2 V^{-1} s^{-1}; this value is two magnitudes higher than that of the organic-inorganic hybrid perovskites [104].

The transportation of carriers in single $FAPbX_3$ crystals (where X = Br^- and I^-) is enhanced compared with that of $MAPbX_3$, where $FAPbBr_3$ crystals display a five-fold longer carrier lifetime than that of the single $MAPbBr_3$ crystals [105]. At a low excitation fluence of 10.59 μJ cm^{-2}, upon two-photon excitation, single $FAPbI_3$ and $FAPbBr_3$ perovskite crystals have ultralong carrier diffusion lengths of 19.7 and 107.2 μm, respectively [106]. Previous discussions clarified that carriers recombine faster at the surface of the grain than in the bulk morphology in the single $MAPbBr_3$ crystals. The surface recombination lifetime is considerably shortened by one order (i.e., from ~34 to ~1 ns), and the diffusion length is reduced to ~130–160 nm from the bulk value of ~2.6–4.3 μm [107]. Recently, a mixed Sn-Pb iodide low-bandgap perovskite $(FASnI_3)_{0.6}(MAPbI_3)_{0.4}$ has received considerable interest for its excellent performance in tandem architecture solar cells with a newly recorded PCE of 25%, which has a long carrier lifetime of 255 ns [108]. After $C_2H_4N_4S$ is added to decrease the defect density, the carrier lifetime surpasses 1 μs, with a long carrier diffusion length of 2.5 μm [5].

Tunability of carrier recombination and transport

Microstructures

Carrier recombination and diffusion dynamics strongly correlate

with the microstructure of solution-processed films, including GB, GS, and defects. As the nonradiative charge recombination centers are most densely located in the regions near GBs, the quality of GBs should be optimized to increase the PL intensity and radiative recombination rate. The larger the GS of the perovskite films, the smaller the proportion of GBs and defect concentration. When the GS increases, the nonradiative recombination rate is suppressed. Studies on the carrier dynamics at a specific area using microTRPL have revealed that the nonradiative decay of GBs is faster than those of other areas, as shown in Fig. 6a, b [109]. In perovskite polycrystalline thin films, surface recombination at the top and bottom plays a more important role in limiting the total carrier lifetime than the recombination inside grains or at GBs. The crystal quality can be improved by reducing the microstrain in a polycrystalline film and introducing aluminum acetylacetonate to a perovskite precursor. Consequently, the nonradiative recombination rate decreases [110]. Adding hypophosphorous acid into the precursor considerably enhances the film quality, with the average GS being enlarged from 168 to 769 nm [111]. A vapor-induced intermediate phase strategy is used to manipulate the morphological characteristics of perovskite films [112]. A compositional/structural conversion of $MAPbI_3$ to PbI_2 occurs mostly at GBs *via* thermal annealing, which hinders the carrier recombination at GBs and enhances the performance of the organic/inorganic hybrid perovskite [113].

Composition

The chemical compositions and stoichiometric ratios in hybrid perovskites are effective parameters to tune the carrier dynamics. Bu *et al.* [114] proposed a quadruple cation perovskite absorber, namely, $K_xCs_{0.05}(FA_{0.85}MA_{0.15})_{0.95}Pb(I_{0.85}Br_{0.15})_3$ (KCsFAMA), with a uniform GS of up to 1 μm, which is approximately two times that of the K-free structure. A longer carrier lifetime indicates fewer irradiative defects because K incorporation produces a higher crystallinity than those of pristine FAMA and CsFAMA perovskites. In three Pb-halide perovskites, i.e., $MAPbI_3$, $FAPbI_3$, and $CsPbI_3$ [115], carriers relax more slowly in $CsPbI_3$ than in the other two perovskites because of the reduced electron-phonon coupling caused by the weak interaction between the Cs cation and the PbI_6 framework. Appropriate $MAPbCl_3$-$MAPbBr_3$ heterojunctions can dramatically reduce the recombination channels in the surface region [116]. In the pristine $FAPbI_3$ perovskite, FA^+ decays to 50% maximum when considering a time constant of 2 ps by a vector autocorrelation function, and the time constant is increased to ~5 ps in mixed $FA_{0.9}A_{0.1}PbI_3$ (A = Cs and Rb) [117]. In the $MAPbI_3$ perovskite, the carrier lifetime increases with the excess PbI_2 [118]. The PL recombination rate slightly decreases from 15 μs^{-1} at a non-stoichiometric ratio of 3:1 of MAI to PbI_2 compared with that of 14 μs^{-1} at a stoichiometric ratio of 1:1 [83]. In an MAFA-mixed solar cell absorber, TRPL measurements have shown that the lifetime roughly increases as the Rb fraction increases, as shown

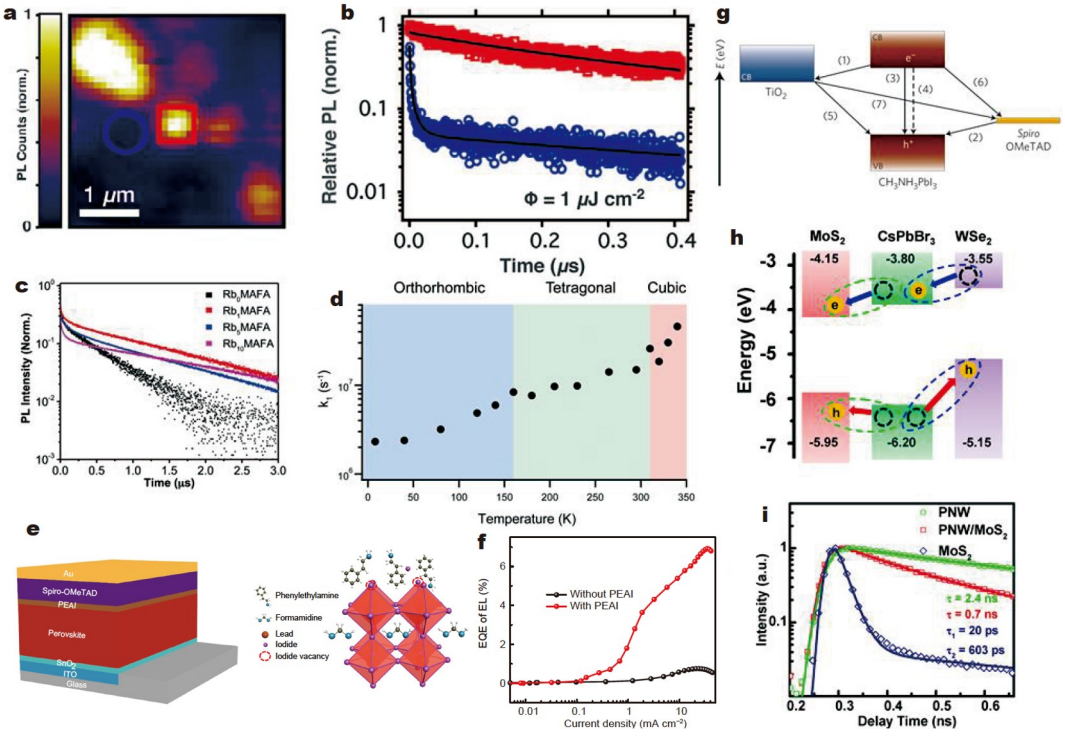

Figure 6 Tunability of carrier dynamics. (a) The blue circle and the red square show dark and bright microstructures and (b) the corresponding carrier lifetime *via* the TRPL measurement. Reprinted with permission from Ref. [109]. Copyright 2015, American Association for the Advancement of Science. (c) Carrier lifetime *versus* the increased Rb fraction in the MAFA-mixed perovskite. Reprinted with permission from Ref. [119]. Copyright 2018, Royal Society of Chemistry. (d) Temperature dependence of the monomolecular recombination rate. Reprinted with permission from Ref. [103]. Copyright 2015, Wiley-VCH. (e) Surface passivation of perovskite film and (f) external quantum efficiency (EQE) of electroluminescence (EL) of the devices with/without a passivation layer. Reprinted with permission from Ref. [126]. Copyright 2019, Springer Nature. (g) Representation of energy levels and electron transfer in an HTM/perovskite/ETM cell, where HTM represents hole transport material and ETM represents electron transport material. Reprinted with permission from Ref. [127]. Copyright 2014, Springer Nature. (h) Band alignments of MoS_2/$CsPbBr_3$/WSe_2 heterostructures, where the arrows indicate the charge transfer pathways. (i) TRPL traces of isolated $CsPbBr_3$, monolayer MoS_2, and $CsPbBr_3$ in a heterostructure. PNW: perovskite nanowire. Reprinted with permission from Ref. [30]. Copyright 2018, American Chemical Society.

in Fig. 6c [119]. Chemical doping is an effective method to tune carrier dynamics. Until now, numerous chemical components have been designed as additives, such as metal ion additives (K^+ [120], Bi^{2+} [121], Sr^{2+} [122], and Al^{3+} [110]) and anion additives (Cl^- [123] and Br^- [124]) in MAI (only at a low concentration of 3%–4%). The nonradiative recombination rate is suppressed using Al^{3+}. Yang *et al.* [22] proposed to introduce additional iodide ions into an organic cation and found that the concentration of deep-level defects decreased.

Temperature-induced phase transition

In the previous section, it was shown that temperature can induce phase transitions in $MAPbI_3$ perovskites, consequently exacerbating crystal disorder with increasing temperature. The monomolecular recombination rate (k_1) increases as temperature increases (Fig. 6c); conversely, bimolecular and Auger recombination rates (k_2 and k_3) decrease as the temperature increases [103]. The carrier dynamics revealed by TRPL have shown that the decay at 22°C is fitted using a biexponential function to be τ_1 = 5.7 ns and τ_2 = 83 ns; at −223°C, the constant is fitted to be τ_1 = 375 ns and τ_2 = 5367 ns; at −268°C, the constant is fitted to be τ_1 = 263 ns and τ_2 = 5043 ns [12]. In a working solar cell, the carrier transport lifetime increases from 2.05 ± 0.06 μs to 2.367 ± 0.05 μs, when the temperature increases from −20 to 25°C, corresponding to the PCE from 14.8% to 13.4% [125]. This prolonged carrier lifetime and decreased PCE are attributed to the decreased carrier mobility with increasing temperature.

Defects and passivation

Carrier recombination at defects limits the performance of perovskite-based photoelectronic devices. The carrier recombination lifetime is limited by trap states at low carrier densities under typical solar illumination, which helps explain why the carrier lifetimes of solution-processed thin films are usually shorter than those of single crystals [128]. When treated with light and a specific atmosphere, a crystalline perovskite can have a carrier lifetime comparable to that of a single crystal [129]. The existence of defects can yield deep or low defect energy and form recombination centers. Most defects have low energy. To some extent, these defects influence the carrier recombination dynamics and diffusion length and eventually determine the device performance [130]. Surface-defect passivation is effective in enhancing the PCE and stability of the perovskite-based solar cells [131]. Many passivation strategies have been proposed to suppress defects, such as thermal annealing [113,132] and using guanidinium-based additives [133], Lewis bases [128,134,135], and ammonium halide anions and cations [136].

Through thermal annealing, MAI is structurally converted to PbI_2 at the GBs of the film, which impedes the carrier recombination at the GBs of the planar heterojunction. PL quenching shows a single-exponential decay trend of 3.65 ns without any annealing; then, it is modified to a biexponential decay with annealing. The longest PL time constants are τ_1 = 6.39 ns and τ_2 = 101.3 ns at the annealing time of 60 min [113]. The surface passivation of a perovskite film is a good approach to modify the carrier dynamics (Fig. 6e). The passivation effect caused by the guanidinium-based additives in $MAPbI_3$ prolongs the perovskite's carrier lifetime by one magnitude longer than that of a pure MA film [133]. The reduced defects at GBs reduce the nonradiative recombination rates, enabling the long carrier diffusion and enhanced PL/EL efficiency, as shown in Fig. 6f. Defects are passivated in an $MAPbI_3$ hybrid perovskite using ammonium halide anions and cations, inducing the reduction of GB defects and prolonging the radiative recombination time from 82.3 to 903.4 ns [136]. The average lifetime of a perovskite film increases from 24 to 40 ns after $NH_3I(CH_2)_8NH_3I$ treatment, revealing the suppressed charge recombination in the treated film [137].

Under illumination, photoinduced halide migration in triiodide perovskites reduces the trap-state density by one order of magnitude. De Quilettes *et al.* [138] found a photoinduced "brightening" of the PL and prolonged carrier recombination in a $MAPbI_3$ perovskite film, which was attributed to defect migration. Mosconi *et al.* [139] proposed the computational modeling of defect migration under light irradiation, promoting the annihilation of Frenkel pairs, which are abundant in polycrystalline $MAPbI_3$. This process partly restores a nondefective crystalline environment and eliminates the trapping centers associated with such defect pairs. A light-induced PL intensity enhancement, and lifetime increasement is also found in surface-deposited $MAPbI_3$ perovskites. The intensity increases up to three orders of magnitude upon light illumination with an excitation power density of 0.01–1 W cm^2, and the lifetime prolongs from several nanoseconds to several hundred nanoseconds [140].

Interfacial charge transfer

After photon excitation, charge carriers are generated from perovskite films, undergoing long-lived carrier relaxation and bipolar transport. Then, carriers should be accepted by the electron/hole-accepted layers and generate an efficient photocurrent. To a large extent, the efficiency of harvesting charge carriers using ETLs/HTLs determines the performance of the device. Once electrons or holes are collected by the extracting layers, the carrier density in the perovskite absorbers decreases, which can be resolved by decreasing PL intensities and increasing carrier lifetimes. The model of electron transfer in a hole transport material (HTM)/perovskite/electron transport material (ETM) cell is shown in Fig. 6g. Here, we summarize how the electron/hole transporting layers affect the carrier extracting efficiency.

The ETL is an n-type semiconductor, and the HTL is a p-type semiconductor. Phenyl-C_{61}-butyric acid methyl ester (PCBM) is the most widely applied electron-accepting layer in a perovskite solar cell. PCBM is an effective candidate that can considerably quench the PL intensity, resulting in a lifetime of 6.1 ± 0.1 ns, compared with a pure $MAPbI_{3-x}Cl_x$ film on poly(methylmethacrylate) (PMMA) with a quenched lifetime of 272.7 ± 7.0 ns; a similar result is observed in a hole acceptor, i.e., spiro-OMeTAD, whose lifetime is quenched to 9.6 ± 0.3 ns [98]. They have been widely applied to various perovskite absorbers ($FAPbI_3$ [58]) and structures. Heavily p-doped $Ni_xMg_{1-x}O$ and n-doped TiO_x charge extraction layers are used in fast and efficient charge carrier extraction. The long carrier recombination of 110.3 ns in a pure $MAPbI_3$ film is shortened to 6.2 ns with a NiO hole-accepting layer and 5.2 ns with a $Li_{0.05}Mg_{0.15}Ni_{0.8}O$ electron extraction layer [9]. Yang's group [141] reported improved air stability of a perovskite solar cell with a metal-oxide transport layer to enhance the stability compared with those of the conventional transport layer (where the PL decays for a pristine $MAPbI_3$ film on glass with NiO_x), spiro-OMeTAD

HTLs, and ZnO, TiO_2, and PCBM ETLs. Without a quenching layer on pure glass, the carrier lifetime is determined to be 145 ns. Then, it decreases to 70 and 21 ns in the presence of NiO_x and ZnO, respectively. The charge extracting ability of the PCBM/spiro-OMeTAD layers is stronger than that of NiO_x/ZnO; they contribute to the stability of working solar cells. Heo *et al.* [142] found that the PL quenching in the glass/$MAPbI_3$/PCBM film (τ_{avg} = 1.28 ns) is faster than that in the F-doped tin oxide (FTO)/TiO_2/$MAPbI_3$ film (τ_{avg} = 1.94 ns), confirming the faster transfer of charge carriers from $MAPbI_3$ into a PCBM electron conductor than into a TiO_2 electron conductor. Zheng *et al.* [143] proposed a mesoporous TiO_2 ETL, which performs a better electron transport than a conventional planar structure, as evidenced by the PL lifetime (6.1 and 7.0 ns, respectively). Adding Ni to rutile TiO_2 is an effective approach to enhance the electron extraction ability with a PL lifetime from 57.4 to 43.8 ns [144]. Adding SnO_2 as a layer in $HC(NH_2)_2PbI_3$-based perovskites affords efficient electron extraction because charge carriers are more rapidly cultivated than a TiO_2 layer [145]. Yang *et al.* [146] found an enhanced ethylene diamine tetraacetic acid-complexed SnO_2 electron transporting layer, which has a higher electron extraction capability than the pure SnO_2 layer. Therefore, the efficiency of carrier collection in graphene-doped mesoporous TiO_2 is increased twice in terms of standard mTiO_2 [147].

An HTL, a functional layer with a CBM higher than the absorber, and an ETM are used to extract holes. Many p-type semiconductors, including organic semiconductors, spiro-OMeTAD [98], PEDOT:PSS [96], Trux-OMeTAD [148], and π-conjugated organic small molecule 4,4′-cyclohexylidenebis[*N*,*N*-bis(4-methylphenyl)benzenamine] [149], have been designed as HTMs. Huang *et al.* [148] reported that the efficiency of Trux-OMeTAD is higher than that of PEDOT:PSS as an HTL; the average PL quenching times are 39.1 and 76.6 ns, and the collecting efficiency is confirmed through the PV performance. A dopant-free polymeric HTM based on benzo[1,2-*b*:4,5:*b*′]-dithiophene and 2,1,3-benzothiadiazole [150] was proposed as an excellent candidate with a better charge extraction ability than the traditional spiro-OMeTAD. In addition to the energy transfer between perovskite and ETL/HTL, other 2D semiconductors have been reported because of their unique optical properties [30]. In perovskite nanowire/2D MoS_2 and WSe_2, which form types I and II heterojunctions (Fig. 6h), ultrafast charge transfer is confirmed using PL spectra and TRPL traces. In the former configuration, the electron and hole transfer from a perovskite nanowire to MoS_2 causes considerable PL quenching and shortens the PL lifetime, as shown in Fig. 6i. Work function can be controlled *via* defect engineering, thereby enabling an ultrafast hole transfer between the MoS_2 monolayer and the $CH_3NH_3PbI_3$ perovskite [151].

ROLE IN DEVICE APPLICATIONS

Opto-electrical conversion

Perovskites have been widely considered for use in various devices, particularly as absorbers in solar cells for the PCE breakthrough. Fig. 7a, b show the perovskite-based solar cell module and device structure, respectively. Long carrier recombination lifetimes and diffusion length of pristine perovskite absorbers are the requisites of high-performance solar cells. Appropriate ETL and HTL should be designed to harvest the photocurrent at the interface between absorbers and transport layers effectively. Charge extraction efficiency can be revealed by the reduction of carrier recombination time for a bilayer perovskite/ETL or a perovskite/HTL; therefore, the shorter the lifetime, the higher the efficiency.

The PCE of a solar cell (η) is determined by multiplying the open-circuit voltage (V_{OC}), short-circuit current density (J_{SC}), and fill factor (FF):

$$\eta = \frac{V_{OC} \times J_{SC} \times FF}{P_{in} \times S}, \tag{6}$$

where P_{in} and S are the power of the incident light and the effective area, respectively. For a given sunlight condition, increasing V_{OC}, J_{SC}, or FF can improve the PCE of a solar cell. In metal halide perovskite solar cells, a high PCE is mainly attributed to the low loss in potential between a bandgap and the open-circuit voltage (E_g/e-V_{OC}). The maximum V_{OC} of a solar

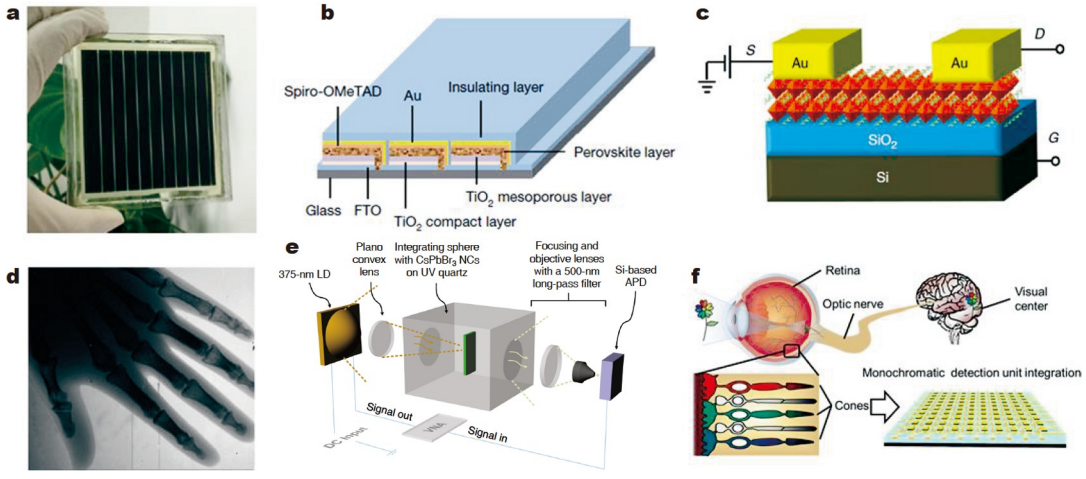

Figure 7 Opto-electrical devices. (a) Solar cell module and (b) device structure. Reprinted with permission from Ref. [156]. Copyright 2017, Springer Nature. (c) Field-effect transistors based on a single-crystal perovskite and output performance. Reprinted with permission from Ref. [157]. Copyright 2018, Springer Nature. (d) X-ray detection. Reprinted with permission from Ref. [158]. Copyright 2017, Springer Nature. (e) High-speed all-inorganic $CsPbBr_3$ perovskite-based PD for ultraviolet light communication. Reprinted with permission from Ref. [159]. Copyright 2019, Springer Nature. (f) Perovskite PD array for applications in image sensors for artificial vision. Reprinted with permission from Ref. [160]. Copyright 2018, American Chemical Society.

cell is dominated by the Shockley-Queisser (SQ) limit V [50]. In $MAPbI_3$ (E_g = 1.5 eV), this value is ~280 meV [152]. The voltage loss in a perovskite solar cell can be partially attributed to the nonradiative recombination [153].

$$\Delta V_{OC}^{nr} = -\frac{kT}{q}\ln\left(EQE_{EL}\right), \quad (7)$$

where $k$is the Boltzmann constant, q is the elemental charge, and EQE_{EL} is the EQE of electrical luminescence. Abdi-Jalebi *et al.* [120] demonstrated high external PL quantum yields in a $(Cs_{0.06}FA_{0.79}MA_{0.15})Pb(I_{0.85}Br_{0.15})_3$-passivated triple-cation perovskite, providing the elusive combination of high luminescence and excellent charge transport. When a certain percent of passivated K^+ is added to a perovskite, the PL quantum efficiency enhances from 41% to 66%, corresponding to the prolonged PL recombination lifetime and reduced potential loss (from 0.26 to 0.11 eV). Although solution-processed perovskite absorber films suffer from the non-negligible density of subgap defect states, the radiative efficiency is usually high in poly- and monocrystalline films, which ensure low nonradiative loss and good performance in solar cells and LEDs. The SQ model describes the relation of V_{OC}, film thickness, and effective carrier lifetime as follows [154]:

$$V_{OC} = \frac{kT}{q}\ln\left(\frac{J_{SC}}{J_0}\right) = \frac{kT}{q}\ln\left(\frac{J_{SC}N_D\tau_{eff}}{qn_i^2 d}\right), \quad (8)$$

where J_0, N_D, τ_{eff}, n_i, and d are the initial current density, doping concentration, effective carrier recombination lifetime, intrinsic carrier concentration, and thickness of the light absorber, respectively. A longer carrier recombination lifetime is beneficial for a larger V_{OC} because it enables a higher carrier concentration [155]. The passivation effect caused by the guanidinium-based additives in $MAPbI_3$ prolongs the carrier lifetime by one magnitude greater than that of the pure MA film [133]. The reduced defects at GBs reduce the nonradiative recombination rates, enabling the long carrier diffusion. V_{OC} improves from 1.025 to 1.071 V; consequently, PCE increases from 16.35% to 17.13%. As 3D perovskites possess a small exciton binding energy of tens of millielectronvolts, the potential offset to dissociate the exciton is quite low, enabling the large V_{OC}.

In addition to the great success in PV, organic-inorganic hybrid and all-inorganic perovskites have been widely considered for PDs because they have a large absorption coefficient, high carrier mobility, and tunable absorption bands, which satisfy the requirement for highly sensitive and broadband PDs. Similar to solar cell absorbers, highly sensitive PDs require a facile exciton into free charge and long carrier diffusion length to achieve efficient charge extraction. Bulk perovskites possess a low exciton binding energy, i.e., only tens of millielectronvolt, following the Wannier model. This value is usually lower than or comparable to the thermal energy at room temperature (25 meV), thereby enabling effective free charge and photocurrent generation. With excellent photoinduced carrier properties, different types of perovskite-based PDs have been proposed; some of them are photodiodes [161–166], photoconductors (Fig. 7c) [167–169], and transistors [157,170–173]. Photoconductive gain means that an incident photon triggers multiple electrons through impact ionization. An efficiency of >1 is possible based on the ratio of the charge recombination time (τ_r) and the charge transit time (τ_t). A high gain can improve the sensitivity of PDs using semiconductors with a long carrier lifetime, high carrier mobility, and a reduced distance between electrodes. Direct-bandgap perovskites have a long carrier lifetime by tens to hundreds of nanoseconds [108] and even up to >1 μs [5,119]. Zou *et al.* [174] reported a vertical structure with a short electrode distance of ~2.3 μm, which enables effective charge extraction and high photoresponsivity of >1000 A W^{-1} at a low incident intensity of 0.66 mW cm^{-2} and a bias voltage of 3 V. Its photoconductive gain is approximately 2.37×10^3, which is attributed to the fast charge transfer and long carrier recombination lifetime.

In PV detectors, the response time is determined by the carrier transit time rather than the carrier recombination lifetime, resulting in a faster response time than that of photoconductors. The typical response time of a PV structure is tens to hundreds of nanoseconds, whereas the response time of the latter is in microseconds or even milliseconds. Li *et al.* [175] reported a fast perovskite/organic PD with a response time of as short as 5.6 ns. A tunable bandgap using chemical or material strategies enables not only the formation of multijunction solar cells but also the development of broadband PDs. Thus far, the spectral range of perovskite-based PD has covered the ultraviolet to near infrared range. A hybrid perovskite has a typical bandgap of electronvolts. Perovskites have been used for sensitive X-ray detection (Fig. 7d) [158,176]. The broad tunable spectral detection and fast response time of perovskite-based PDs are the desired characteristics for fast optical communication (Fig. 7e), rapid imaging for artificial vision (Fig. 7f), and high-speed dynamic process monitoring.

Electro-optical conversion

Electro-optical conversion enables the use of LEDs (Fig. 8a) and laser diodes if a Fabry-Perot cavity is incorporated. As discussed above, an efficient PCE in perovskite-based solar cells requires long carrier diffusion length and facile exciton dissociation into a free carrier. A direct-bandgap perovskite has high PL quantum yields, which indicates an efficient multicolor display. Similar to solar cells, highly efficient light emission requires low nonradiative recombination, as revealed by a low defect concentration and a long carrier lifetime [177]. However, factors limit the EL efficiency of LEDs that differ from PV devices: (1) substantial luminescence quenching caused by the thermal ionization of excitons generated in an absorber layer and (2) a large GS and a rough nonuniform surface inducing long carrier diffusion length and substantial leakage. Therefore, improving the EL efficiency and tuning the emission band are the primary targets for LEDs and laser diodes.

An efficient PL is a prerequisite for high-performance LEDs. PL yield can be enhanced through light curing with oxygen [140], anion exchange [31], thickness tailoring [178–180], improvement of light extraction on nanophotonic substrates [181], surface passivation [179], chemical compounding [32,35,182], and temperature control [34]. Carrier lifetime, together with the PL intensity, can be indicative of achieving high-performance LEDs. The EQE in violet EL is improved by converting polycrystalline thin films to $(PEA)_2PbBr_4$ nanoplates *via* solvent vapor annealing [180]. The modified nanoplates show a carrier lifetime of 1.27 ps, which is two times longer than that of the thin film; this finding indicates lower nonradiative recombination, which can be confirmed by the PL intensity (quantum yield= 26% for nanoplates and 10% for thin film). For LED performance, the EQE of devices based on thin films is as

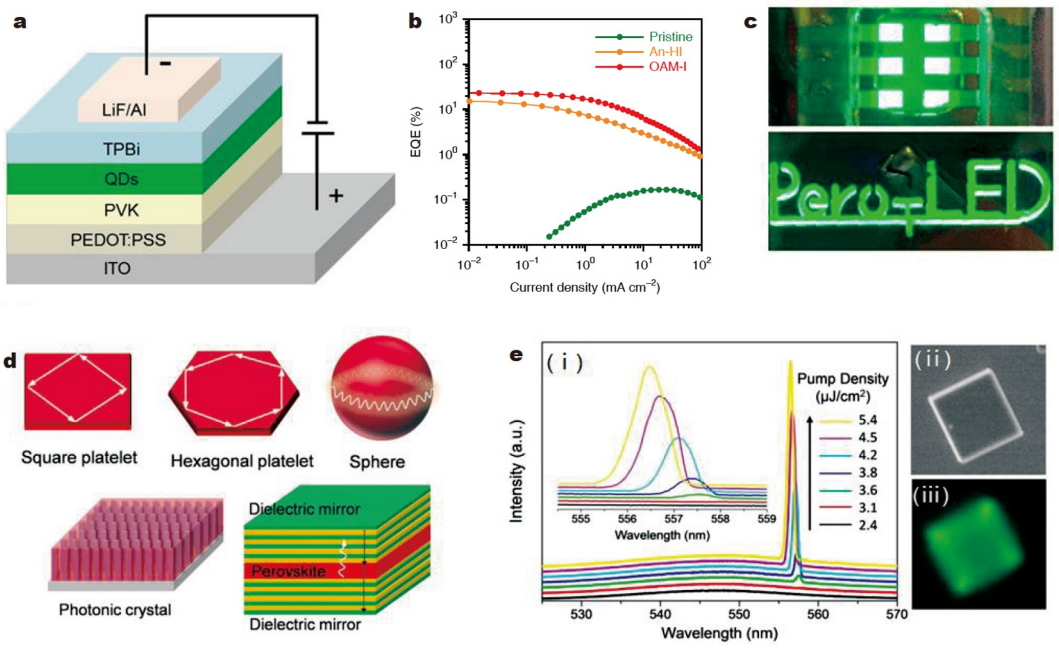

Figure 8 Electro-optical devices. (a) Illustration of a multilayer perovskite QD LEDs (QLED). Reprinted with permission from Ref. [186]. Copyright 2015, Wiley-VCH. (b) EQE of anion-exchange $CsPbBr_3$ perovskite QDs *versus* the pristine situation. Reprinted with permission from Ref. [31]. Copyright 2018, Springer Nature. (c) Photograph of a perovskite-based blue LED. Reprinted with permission from Ref. [187]. Copyright 2018, Springer Nature. (d) Schematic of perovskite lasers formed by different cavities. Reprinted with permission from Ref. [188]. Copyright 2017, Wiley-VCH. (e) MicroPL spectra of a square microdisk (i), as shown in (ii), *versus* the excitation density. (iii) MicroPL image of the square microdisc. Reprinted with permission from Ref. [189]. Copyright 2015, Wiley-VCH.

low as 0.002% and enhanced to 0.008% on nanoflakes. Excessive Pb atoms in $MAPbBr_3$ increase the nonradiative recombination and degrade luminescence [183]. Cho *et al.* [184] found that a slight increase in the excessive MABr with a stoichiometric ratio of $MABr:PbBr_2$ = 1.05:1 can improve the radiative recombination and decrease the carrier diffusion length. As a result, the current efficiency of the target LEDs improves to 42.9 cd A^{-1} compared with 0.183 cd A^{-1} at a ratio of 1:1. Anion-exchange perovskite QD-based LEDs exhibit a high EQE of up to 21.3%, whereas pristine $CsPbBr_3$ QDs have an EQE of 14.1% [31], as shown in Fig. 8b. This enhancement is attributed to the reduction of anion defect formation [185].

Tunable light emission wavelengths covering the visible band from blue to red have been achieved in perovskite QDs [31,32,34,35,186] and 2D morphology [66,182,190–193]. Fig. 8c shows the photograph of an efficient perovskite-based blue LED [187]. Color tuning is mainly achieved by size-related quantum confinement or chemical compound. In an $MAPbI_{3-x}Br_x$ perovskite thin film, the full-band gap range of 1.6–2.3 eV is achieved by adjusting the ratio of PbI_2 and $PbBr_2$ [194]. A bright PL with a narrow bandwidth of tens of nanometers ensures pure color emission. In MA_3BiX_9 (X = Cl, Br, and I) QDs, the emission wavelength is considerably tuned using different halide compositions, i.e., 360 nm for MA_3BiCl_9, 423 nm for MA_3BiBr_9, and 540 nm for MA_3BiCl_9 [35]. Similar composition tunable emission occurs in perovskite $CsPbX_3$ QDs [186] and 2D nanosheets [195]. Huang *et al.* [34] found that the emission color of $MAPbBr_3$ perovskite QDs is achieved by precipitation temperature. The emission peak in the range of 475–520 nm is obtained by changing the temperature from 0 to 60°C. Additionally, the wavelength can be tuned by varying the thickness of 2D perovskites, such as $(PEA)_2SnI_xBr_{4-x}$ [193], $(MA)_{m-1}Pb_mBr_{3m+1}$ [192], $BA_2FA_{n-1}Pb_nBr_{3n+1}(n = 2–5)$ [196], $BA_2MA_{n-1}Pb_nBr_{3n+1}$ [58,162], and $BA_2MA_{n-1}Sn_nI_{3n+1}$ [38]. Organic LEDs represent the next-generation display technology. Hybrid perovskites possess the advantage of organics for flexibility, easy fabrication, and overcoming the disadvantage of low carrier mobility. An extraordinarily thick $CH_3NH_3PbCl_3$ ($MAPbCl_3$) transport layer is used instead of the pure organics to considerably reduce the voltage of high carrier mobility and make the layer transparent to visible light [197]. The hole mobility is 1.3 cm^2 V^{-1} s^{-1} (for L = 3000 nm), and the electron mobility is 2.9 cm^2 V^{-1} s^{-1} (for L = 3000 nm), which is 10^3 times more than the value of conventional organic films.

A laser output requires an efficient EL and suitable cavity design to amplify stimulation emission. Perovskites have achieved great success in LEDs, and their successful application in electroexcitation nanolasers is anticipated. Most perovskite-based lasers are achieved by optical pumping, while the electroexcitation is rarely reported. Various cavity structures have been designed [198]; some of them include whispering-gallery-mode cavities [199,200], Fabry-Perot nanowire cavities, QD structures, and thin films, as shown in Fig. 8d. In addition to down-conversion lasers, two-photon up-conversion lasers are achieved for high nonlinearity [200,201]. Carrier dynamic evolution can be used to monitor the laser working mode. Under low excitation, a monomolecular recombination mechanism dominates recombination, accompanied by long and single carrier dynamics. Fast recombination occurs when excitation energy increases.

All-optical conversion

Energy is inevitably wasted during electro-optical and opto-electrical conversion processes. To some extent, all-optical

conversion is a good approach to eliminate energy wastage. A large absorption coefficient and a strong light-matter interaction cause excellent nonlinear effects on perovskites, thereby promoting all-optical device applications. All-optical conversion incorporates PL, harmonic generation, frequency conversion, optical switching, and saturable absorption. Despite a non-negligible defect concentration, perovskite possesses a high PL efficiency of a low nonradiative recombination rate. In contrast to EL, such as in LED, PL is easily generated in direct-bandgap perovskites. The relation between exciton energy and emission energy is dominated by the Stokes ($h\nu_{ex} > h\nu_{em}$) or anti-Stokes ($h\nu_{ex} < h\nu_{em}$) law. By the Stokes law, the PL of perovskite, as fundamental and robust characterization spectroscopy, has been intensively investigated in the past years (Fig. 9a). By comparison, two-photon or multiphoton PL (Stokes law) has been widely explored because of its unique advantages, including high-resolution and high signal-to-noise ratio imaging. A large two-phonon absorption coefficient of up to 221.5 cm MW^{-1} is observed in a 2D perovskite, which is ~3–4 magnitudes larger than those of the conventional semiconductor QDs (CdSe) and 2D semiconductors (WS_2 monolayer) [202]. Strong two-phonon absorption enables bright two-photon pumped PL [203] and nanolasers [199,200,204]. In addition to two-phonon absorption, multiphoton absorption has been found. Chen *et al.* [205] reported a large five-photon absorption in core-shell structured perovskite NCs, as shown in Fig. 9b. Multiphoton absorption is important for *in vivo* imaging and optical limiting. In biophotonics, perovskites have been applied to multiplex cellular imaging. In optical modulators and switches based on a nonlinear effect, modulation depth and lifetime are the key parameters for a high signal-to-noise ratio and high-speed manipulation. Wu *et al.* [206] reported an optical switch based on the self-phase modulation of space, where a strong green laser beam (λ = 532 nm) is used to control a blue beam (λ = 457 nm). The schematic and output performance plot of $CsPbX_3$-all-optical switching are shown in Fig. 9d, e, respectively. A terahertz modulator is obtained using a $CsPbBr_3$ perovskite QD heterostructure [207] and an all-optical terahertz wave switch based on a $MAPbI_3$ perovskite [208]. Perovskites are applied to ultrafast photonics as the slow SAs. Saturable absorption indicates that the absorption coefficient decreases as the input fluence increases. Upon high excitation, it causes "optical bleaching", as shown in Fig. 9f. For a slow SA, the carrier response time can be made longer than the generated ultrafast pulses by passive mode-locking in an optical cavity. In comparison with the fast SA switched *via* the Kerr effect on Ti:sapphire ultrafast lasers, passive mode-locking employs slow SA to relieve the cavity working at the steady edge and facilitate self-starting. However, the modulation depth is smaller than that of the Kerr-effect-induced fast SA. It is still an effective way to generate pulses

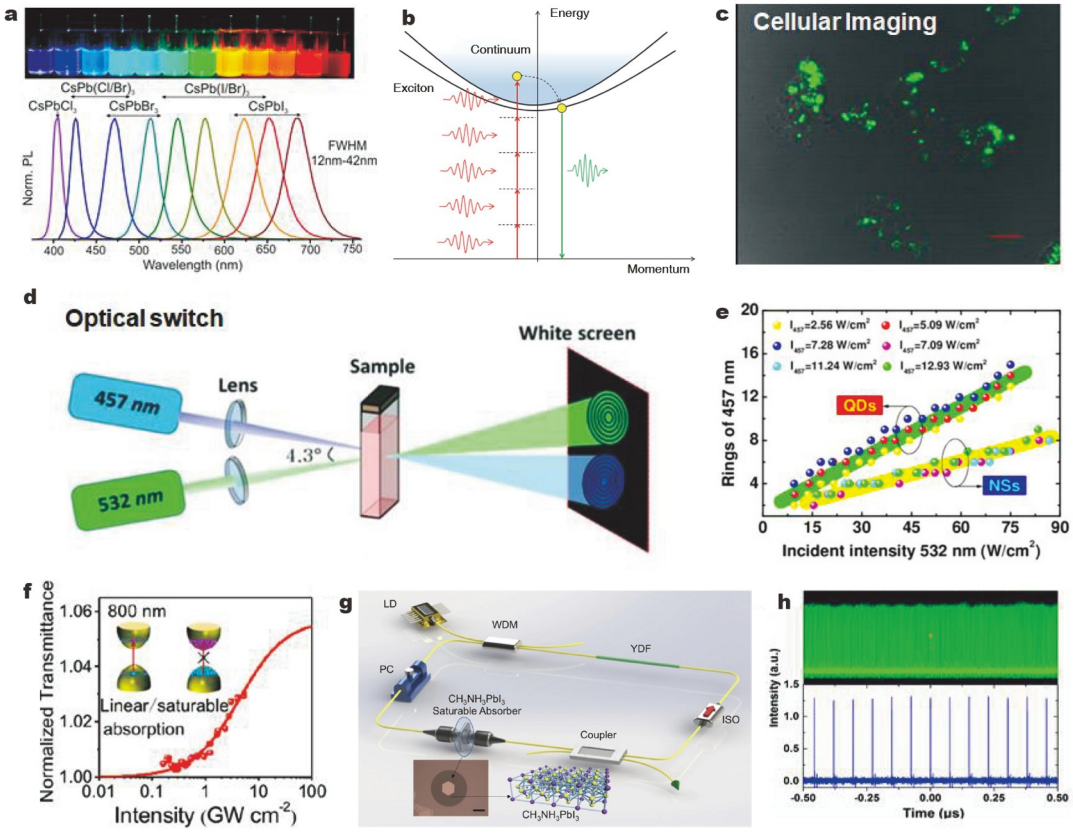

Figure 9 (a) PL spectra of all-inorganic colloidal solutions in toluene. Reprinted with permission from Ref. [209]. Copyright 2015, American Cheical Society. (b) Schematic of five-photon PL in perovskite QDs. Reprinted with permission from Ref. [205]. Copyright 2017, Springer Nature. (c) Multiplex cellular imaging and *in vitro* tumor targeting based on perovskite. Reprinted with permission from Ref. [210]. Copyright 2019, American Cheical Society. (d) Schematic of $CsPbX_3$-all-optical switching based on self-phase modulation and (e) output performance. Reprinted with permission from Ref. [206]. Copyright 2018, Wiley-VCH. (f) Mechanism of saturable absorption in perovskites. (g) Schematic of the ring cavity of a $MAPbI_3$-based mode-locked fiber laser. Reprinted with permission from Ref. [211]. Copyright 2017, Springer Nature. (h) Typical pulse trains at different time scales. Reprinted with permission from Ref. [212]. Copyright 2017, American Institute of Physics.

from hundreds of femtoseconds to picoseconds. The developed and optimized perovskites also provide a novel family of candidates applied to this field.

Since 2017, perovskites have been used as slow SAs in ultrafast photonics at 1064 nm [213] and communication band [214]. The typical experimental diagram of passively mode-locked fiber laser based on SA is shown in Fig. 9g. Li *et al.* [211] proposed 2D $MAPbI_3$ perovskite nanosheets for an effective slow SA to generate picosecond pulses working at 1064 nm. Jiang *et al.* [212] achieved 661-fs ultrafast laser pulses (Fig. 9h) at a communication band of 1555 nm. C- and L-bands pulses are generated in an anomalous dispersion regime by adjusting the optical gain with the shortest pulse to 381 fs by employing a novel crystalline $(C_6H_5C_2H_4NH_3)_2PbI_4$ perovskite. In a normal dispersion regime, stable pulses with a signal-to-noise ratio at 89 dB are achieved at a C band [215]. These results suggest that perovskites are potential candidates. Notably, absorption band, damage threshold, tunable modulation depth, and recovering time are critical parameters for an SA. Optimal candidates can be designed by considering perovskites' tunable photoelectronic properties through various strategies. Although the response time of slow SA can be shorter than pulse duration, most of the developed effective SA processes have a short carrier recovery time in the range of femtoseconds to picoseconds. However, tuning the lifetime of perovskites in this range through defect engineering, integrating heterostructure, and other processes is challenging.

CONCLUSIONS AND OUTLOOK

The application of perovskites has been widely extended to solar cells. In photoelectronics, the discovery of photoinduced species and dynamic processes is the basis for achieving high performance; among them, an "effective carrier" is a key factor. In this review, we discuss the fundamentally photoinduced species (free carriers and excitons), tuning strategies (including the tuning of chemical compounds), defect passivation, and charge transfer between heterojunctions (Fig. 10). Free carriers and Coulombic interaction-induced excitons coexist in perovskites, and their fraction is determined using exciton binding energy. In optoelectrical devices, the ease of neutral exciton dissolution facilitates photocarrier collection to achieve high-performance in solar cells and PDs as well as well-known long carrier lifetime and diffusion length. In solar cells and LEDs, defect tolerance and low nonradiative loss help achieve large PCE and high quantum yields. In modulators and switches, introducing defects is an effective approach to shorten the carrier lifetime, enabling high-speed modulation. Bandgap engineering considerably expands the working spectra of devices to achieve short-band X-rays and long-band terahertz responses. Combined studies from the perspective of chemical, physical, and material fields are indispensable to enhance device performance. In these studies, *in situ* photoinduced species and dynamic monitoring should be performed to control "effective carriers" in the devices.

In practical applications of optoelectronic devices, long-term stability is a key factor that determines whether the perovskite-based devices can be commercialized [216,217]. Perovskite stability has two crucial factors: material stability and device stability. For material stability, the perovskite lattice easily breaks down under ambient conditions, particularly when it is exposed to heat and humidity [218]. Suitable elements should be chosen on the basis of tolerance factors to form a stable perovskite lattice [219]. For device stability, many strategies have been

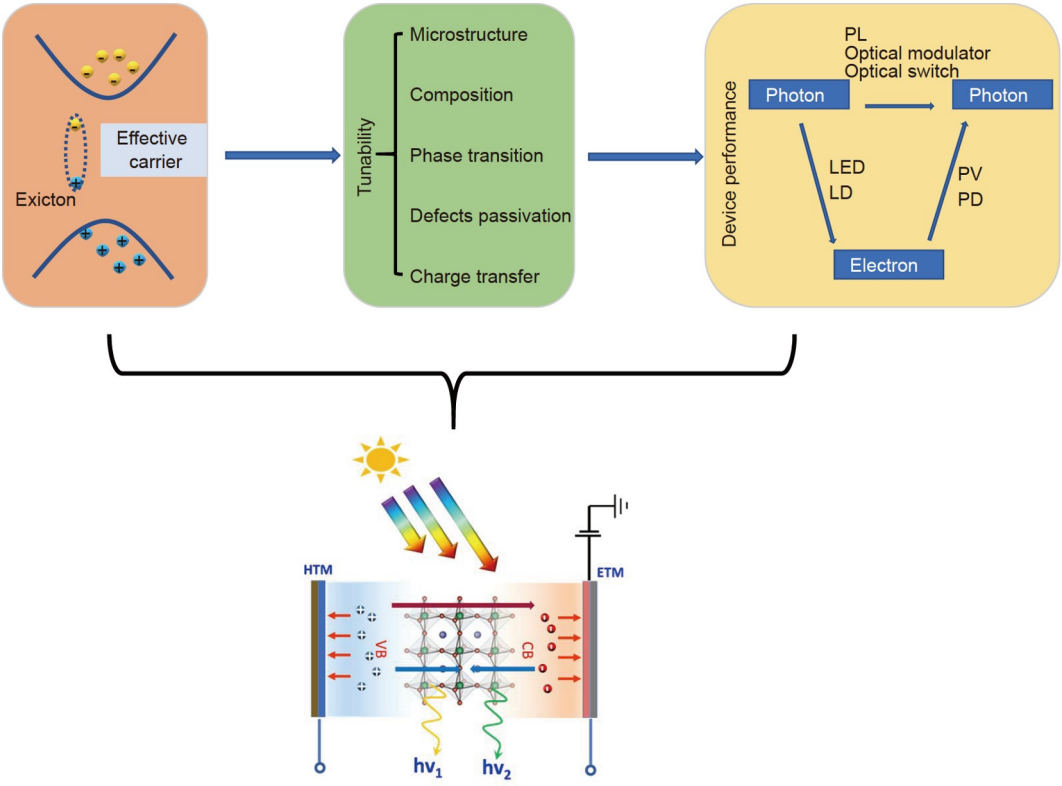

Figure 10 "Effective carrier" in perovskites, tunability, and role in device applications.

proposed from the perspective of atomic substitution [220], interfacial engineering [23,120,221], and the packing technique [222] to solve the stability problem. After years of investigation, the fundamental carrier and exciton dynamics in perovskites have been well understood to a large extent. However, complex multibody interaction remains to be explored. For a strong light-matter interaction in perovskites, especially in low-dimensional limits, all-optical manipulation and related devices should be explored in the future. Fundamentally photoinduced species, including free carriers, excitons, polaritons, and phonons, should be characterized using *in situ* spectroscopic technologies. Another aspect involves actively tuning the dynamics of optical parameters through the abovementioned strategies. For example, in an SA, a much shorter carrier lifetime can be achieved in direct-bandgap semiconductors by introducing defects and suppressing radiative recombination, which helps shape ultrashort pulses. In optical modulators, linear and nonlinear parameters, such as response wavelength, modulation depth, nonsaturable loss, and recovery time, are the key issues that should be controlled to achieve a high performance. Photonic devices at the attractive band of optical communication, mid-infrared, and terahertz band can be achieved by bandgap engineering.

Received 28 September 2021; accepted 24 November 2021; published online 18 January 2022

1 Kojima A, Teshima K, Shirai Y, *et al.* Organometal halide perovskites as visible-light sensitizers for photovoltaic cells. J Am Chem Soc, 2009, 131: 6050–6051
2 BR-CEC. Best research-cell efficiency chart. https://www.nrel.gov/pv/cell-efficiency.html. 2020
3 Wang Y, Dar MI, Ono LK, *et al.* Thermodynamically stabilized β-$CsPbI_3$-based perovskite solar cells with efficiencies >18%. Science, 2019, 365: 591–595
4 De Wolf S, Holovsky J, Moon SJ, *et al.* Organometallic halide perovskites: Sharp optical absorption edge and its relation to photovoltaic performance. J Phys Chem Lett, 2014, 5: 1035–1039
5 Tong J, Song Z, Kim DH, *et al.* Carrier lifetimes of >1 μs in Sn-Pb perovskites enable efficient all-perovskite tandem solar cells. Science, 2019, 364: 475–479
6 Dong Q, Fang Y, Shao Y, *et al.* Electron-hole diffusion lengths >175 μm in solution-grown $CH_3NH_3PbI_3$ single crystals. Science, 2015, 347: 967–970
7 Luo D, Su R, Zhang W, *et al.* Minimizing non-radiative recombination losses in perovskite solar cells. Nat Rev Mater, 2020, 5: 44–60
8 Dar MI, Jacopin G, Meloni S, *et al.* Origin of unusual bandgap shift and dual emission in organic-inorganic lead halide perovskites. Sci Adv, 2016, 2: e1601156
9 Chen W, Wu Y, Yue Y, *et al.* Efficient and stable large-area perovskite solar cells with inorganic charge extraction layers. Science, 2015, 350: 944–948
10 Jung EH, Jeon NJ, Park EY, *et al.* Efficient, stable and scalable perovskite solar cells using poly(3-hexylthiophene). Nature, 2019, 567: 511–515
11 Huang F, Li M, Siffalovic P, *et al.* From scalable solution fabrication of perovskite films towards commercialization of solar cells. Energy Environ Sci, 2019, 12: 518–549
12 Fang HH, Raissa R, Abdu-Aguye M, *et al.* Photophysics of organic-inorganic hybrid lead iodide perovskite single crystals. Adv Funct Mater, 2015, 25: 2378–2385
13 Katan C, Mercier N, Even J. Quantum and dielectric confinement effects in lower-dimensional hybrid perovskite semiconductors. Chem Rev, 2019, 119: 3140–3192
14 Brenner TM, Egger DA, Kronik L, *et al.* Hybrid organic-inorganic perovskites: Low-cost semiconductors with intriguing charge-transport properties. Nat Rev Mater, 2016, 1: 15007
15 Herz LM. Charge-carrier dynamics in organic-inorganic metal halide perovskites. Annu Rev Phys Chem, 2016, 67: 65–89
16 Hutter EM, Eperon GE, Stranks SD, *et al.* Charge carriers in planar and meso-structured organic-inorganic perovskites: Mobilities, lifetimes, and concentrations of trap states. J Phys Chem Lett, 2015, 6: 3082–3090
17 Shi J, Li Y, Li Y, *et al.* From ultrafast to ultraslow: Charge-carrier dynamics of perovskite solar cells. Joule, 2018, 2: 879–901
18 Peng J, Chen Y, Zheng K, *et al.* Insights into charge carrier dynamics in organo-metal halide perovskites: From neat films to solar cells. Chem Soc Rev, 2017, 46: 5714–5729
19 Bi Y, Hutter EM, Fang Y, *et al.* Charge carrier lifetimes exceeding 15 μs in methylammonium lead iodide single crystals. J Phys Chem Lett, 2016, 7: 923–928
20 Chen Y, Yi HT, Wu X, *et al.* Extended carrier lifetimes and diffusion in hybrid perovskites revealed by Hall effect and photoconductivity measurements. Nat Commun, 2016, 7: 12253
21 Wang Y, Chen K, Hao H, *et al.* Engineering ultrafast charge transfer in a bismuthene/perovskite nanohybrid. Nanoscale, 2019, 11: 2637–2643
22 Yang WS, Park BW, Jung EH, *et al.* Iodide management in formamidinium-lead-halide–based perovskite layers for efficient solar cells. Science, 2017, 356: 1376–1379
23 Zhang F, Bi D, Pellet N, *et al.* Suppressing defects through the synergistic effect of a Lewis base and a Lewis acid for highly efficient and stable perovskite solar cells. Energy Environ Sci, 2018, 11: 3480–3490
24 Yin G, Zhao H, Jiang H, *et al.* Precursor engineering for all-inorganic $CsPbI_2Br$ perovskite solar cells with 14.78% efficiency. Adv Funct Mater, 2018, 28: 1803269
25 Li D, Wang G, Cheng HC, *et al.* Size-dependent phase transition in methylammonium lead iodide perovskite microplate crystals. Nat Commun, 2016, 7: 11330
26 Kong L, Liu G, Gong J, *et al.* Simultaneous band-gap narrowing and carrier-lifetime prolongation of organic-inorganic trihalide perovskites. Proc Natl Acad Sci U S A, 2016, 113: 8910–8915
27 Dou L, Wong AB, Yu Y, *et al.* Atomically thin two-dimensional organic-inorganic hybrid perovskites. Science, 2015, 349: 1518–1521
28 Tsai H, Nie W, Blancon JC, *et al.* High-efficiency two-dimensional Ruddlesden-Popper perovskite solar cells. Nature, 2016, 536: 312–316
29 Zhu H, Fu Y, Meng F, *et al.* Lead halide perovskite nanowire lasers with low lasing thresholds and high quality factors. Nat Mater, 2015, 14: 636–642
30 Fang Q, Shang Q, Zhao L, *et al.* Ultrafast charge transfer in perovskite nanowire/2D transition metal dichalcogenide heterostructures. J Phys Chem Lett, 2018, 9: 1655–1662
31 Chiba T, Hayashi Y, Ebe H, *et al.* Anion-exchange red perovskite quantum dots with ammonium iodine salts for highly efficient light-emitting devices. Nat Photon, 2018, 12: 681–687
32 Makarov NS, Guo S, Isaienko O, *et al.* Spectral and dynamical properties of single excitons, biexcitons, and trions in cesium-lead-halide perovskite quantum dots. Nano Lett, 2016, 16: 2349–2362
33 Pan J, Sarmah SP, Murali B, *et al.* Air-stable surface-passivated perovskite quantum dots for ultra-robust, single- and two-photon-induced amplified spontaneous emission. J Phys Chem Lett, 2015, 6: 5027–5033
34 Huang H, Susha AS, Kershaw SV, *et al.* Control of emission color of high quantum yield $CH_3NH_3PbBr_3$ perovskite quantum dots by precipitation temperature. Adv Sci, 2015, 2: 1500194
35 Leng M, Chen Z, Yang Y, *et al.* Lead-free, blue emitting bismuth halide perovskite quantum dots. Angew Chem Int Ed, 2016, 55: 15012–15016
36 Shi E, Gao Y, Finkenauer BP, *et al.* Two-dimensional halide perovskite nanomaterials and heterostructures. Chem Soc Rev, 2018, 47: 6046–6072
37 Stoumpos CC, Cao DH, Clark DJ, *et al.* Ruddlesden-Popper hybrid lead iodide perovskite 2D homologous semiconductors. Chem Mater, 2016, 28: 2852–2867
38 Cao DH, Stoumpos CC, Yokoyama T, *et al.* Thin films and solar cells based on semiconducting two-dimensional Ruddlesden-Popper

$(CH_3(CH_2)_3NH_3)_2(CH_3NH_3)_{n-1}Sn_nI_{3n+1}$ perovskites. ACS Energy Lett, 2017, 2: 982–990
39 Zhang L, Liang WZ. How the structures and properties of two-dimensional layered perovskites $MAPbI_3$ and $CsPbI_3$ vary with the number of layers. J Phys Chem Lett, 2017, 8: 1517–1523
40 Yang JH, Yuan Q, Yakobson BI. Chemical trends of electronic properties of two-dimensional halide perovskites and their potential applications for electronics and optoelectronics. J Phys Chem C, 2016, 120: 24682–24687
41 Jiao Y, Yi S, Wang H, *et al.* Strain engineering of metal halide perovskites on coupling anisotropic behaviors. Adv Funct Mater, 2021, 31: 2006243
42 Jiang S, Fang Y, Li R, *et al.* Pressure-dependent polymorphism and band-gap tuning of methylammonium lead iodide perovskite. Angew Chem Int Ed, 2016, 55: 6540–6544
43 Jaffe A, Lin Y, Beavers CM, *et al.* High-pressure single-crystal structures of 3D lead-halide hybrid perovskites and pressure effects on their electronic and optical properties. ACS Cent Sci, 2016, 2: 201–209
44 Wang Y, Lü X, Yang W, *et al.* Pressure-induced phase transformation, reversible amorphization, and anomalous visible light response in organolead bromide perovskite. J Am Chem Soc, 2015, 137: 11144–11149
45 Park NG. Perovskite solar cells: An emerging photovoltaic technology. Mater Today, 2015, 18: 65–72
46 Fu Y, Zhu H, Chen J, *et al.* Metal halide perovskite nanostructures for optoelectronic applications and the study of physical properties. Nat Rev Mater, 2019, 4: 169–188
47 Zhang YY, Chen S, Xu P, *et al.* Intrinsic instability of the hybrid halide perovskite semiconductor $CH_3NH_3PbI_3$. Chin Phys Lett, 2018, 35: 036104
48 Azpiroz JM, Mosconi E, Bisquert J, *et al.* Defect migration in methylammonium lead iodide and its role in perovskite solar cell operation. Energy Environ Sci, 2015, 8: 2118–2127
49 Ball JM, Petrozza A. Defects in perovskite-halides and their effects in solar cells. Nat Energy, 2016, 1: 16149
50 Shockley W, Queisser HJ. Detailed balance limit of efficiency of p-n junction solar cells. J Appl Phys, 1961, 32: 510–519
51 Grancini G, Nazeeruddin MK. Dimensional tailoring of hybrid perovskites for photovoltaics. Nat Rev Mater, 2018, 4: 4–22
52 Manser JS, Kamat PV. Band filling with free charge carriers in organometal halide perovskites. Nat Photon, 2014, 8: 737–743
53 Williams FE, Hebb MH. Theoretical spectra of luminescent solids. Phys Rev, 1951, 84: 1181–1183
54 Menéndez-Proupin E, Palacios P, Wahnón P, *et al.* Self-consistent relativistic band structure of the $CH_3NH_3PbI_3$ perovskite. Phys Rev B, 2014, 90: 045207
55 Miyata A, Mitioglu A, Plochocka P, *et al.* Direct measurement of the exciton binding energy and effective masses for charge carriers in organic-inorganic tri-halide perovskites. Nat Phys, 2015, 11: 582–587
56 Yin WJ, Shi T, Yan Y. Unusual defect physics in $CH_3NH_3PbI_3$ perovskite solar cell absorber. Appl Phys Lett, 2014, 104: 063903
57 Blancon JC, Tsai H, Nie W, *et al.* Extremely efficient internal exciton dissociation through edge states in layered 2D perovskites. Science, 2017, 355: 1288–1292
58 Eperon GE, Stranks SD, Menelaou C, *et al.* Formamidinium lead trihalide: A broadly tunable perovskite for efficient planar heterojunction solar cells. Energy Environ Sci, 2014, 7: 982
59 Even J, Pedesseau L, Katan C. Analysis of multivalley and multibandgap absorption and enhancement of free carriers related to exciton screening in hybrid perovskites. J Phys Chem C, 2014, 118: 11566–11572
60 Slavney AH, Leppert L, Bartesaghi D, *et al.* Defect-induced band-edge reconstruction of a bismuth-halide double perovskite for visible-light absorption. J Am Chem Soc, 2017, 139: 5015–5018
61 Agiorgousis ML, Sun YY, Zeng H, *et al.* Strong covalency-induced recombination centers in perovskite solar cell material $CH_3NH_3PbI_3$. J Am Chem Soc, 2014, 136: 14570–14575
62 Mitzi DB. Synthesis, crystal structure, and optical and thermal properties of $(C_4H_9NH_3)_2MI_4$ (M = Ge, Sn, Pb). Chem Mater, 1996, 8: 791–800
63 Kagan CR, Mitzi DB, Dimitrakopoulos CD. Organic-inorganic hybrid materials as semiconducting channels in thin-film field-effect transistors. Science, 1999, 286: 945–947
64 Sadhanala A, Ahmad S, Zhao B, *et al.* Blue-green color tunable solution processable organolead chloride-bromide mixed halide perovskites for optoelectronic applications. Nano Lett, 2015, 15: 6095–6101
65 McMeekin DP, Sadoughi G, Rehman W, *et al.* A mixed-cation lead mixed-halide perovskite absorber for tandem solar cells. Science, 2016, 351: 151–155
66 Cao DH, Stoumpos CC, Farha OK, *et al.* 2D homologous perovskites as light-absorbing materials for solar cell applications. J Am Chem Soc, 2015, 137: 7843–7850
67 Liu G, Kong L, Gong J, *et al.* Pressure-induced bandgap optimization in lead-based perovskites with prolonged carrier lifetime and ambient retainability. Adv Funct Mater, 2017, 27: 1604208
68 D'Innocenzo V, Grancini G, Alcocer MJP, *et al.* Excitons *versus* free charges in organo-lead tri-halide perovskites. Nat Commun, 2014, 5: 3586
69 Tanaka K, Takahashi T, Ban T, *et al.* Comparative study on the excitons in lead-halide-based perovskite-type crystals $CH_3NH_3PbBr_3$ $CH_3NH_3PbI_3$. Solid State Commun, 2003, 127: 619–623
70 Sun S, Salim T, Mathews N, *et al.* The origin of high efficiency in low-temperature solution-processable bilayer organometal halide hybrid solar cells. Energy Environ Sci, 2014, 7: 399–407
71 Savenije TJ, Ponseca Jr. CS, Kunneman L, *et al.* Thermally activated exciton dissociation and recombination control the carrier dynamics in organometal halide perovskite. J Phys Chem Lett, 2014, 5: 2189–2194
72 Wu K, Bera A, Ma C, *et al.* Temperature-dependent excitonic photoluminescence of hybrid organometal halide perovskite films. Phys Chem Chem Phys, 2014, 16: 22476–22481
73 Yang Y, Ostrowski DP, France RM, *et al.* Observation of a hot-phonon bottleneck in lead-iodide perovskites. Nat Photon, 2015, 10: 53–59
74 Unuchek D, Ciarrocchi A, Avsar A, *et al.* Room-temperature electrical control of exciton flux in a van der Waals heterostructure. Nature, 2018, 560: 340–344
75 Wang X, Jones AM, Seyler KL, *et al.* Highly anisotropic and robust excitons in monolayer black phosphorus. Nat Nanotech, 2015, 10: 517–521
76 Yang Y, Yang M, Zhu K, *et al.* Large polarization-dependent exciton optical Stark effect in lead iodide perovskites. Nat Commun, 2016, 7: 12613
77 Chernikov A, Berkelbach TC, Hill HM, *et al.* Exciton binding energy and nonhydrogenic rydberg series in monolayer WS_2. Phys Rev Lett, 2014, 113: 076802
78 Shi Z, Muhammad S, Deng L, *et al.* Magnetic-brightening and control of dark exciton in $CsPbBr_3$ perovskite. Sci China Mater, 2020, 63: 1503–1509
79 Chen L, Li B, Zhang C, *et al.* Composition-dependent energy splitting between bright and dark excitons in lead halide perovskite nanocrystals. Nano Lett, 2018, 18: 2074–2080
80 Tamarat P, Hou L, Trebbia JB, *et al.* The dark exciton ground state promotes photon-pair emission in individual perovskite nanocrystals. Nat Commun, 2020, 11: 6001
81 Tamarat P, Bodnarchuk MI, Trebbia JB, *et al.* The ground exciton state of formamidinium lead bromide perovskite nanocrystals is a singlet dark state. Nat Mater, 2019, 18: 717–724
82 de Weerd C, Gomez L, Capretti A, *et al.* Efficient carrier multiplication in $CsPbI_3$ perovskite nanocrystals. Nat Commun, 2018, 9: 4199
83 Wehrenfennig C, Eperon GE, Johnston MB, *et al.* High charge carrier mobilities and lifetimes in organolead trihalide perovskites. Adv Mater, 2014, 26: 1584–1589
84 Li X, Bi D, Yi C, *et al.* A vacuum flash-assisted solution process for high-efficiency large-area perovskite solar cells. Science, 2016, 353: 58–62
85 Leijtens T, Eperon GE, Barker AJ, *et al.* Carrier trapping and re-

combination: The role of defect physics in enhancing the open circuit voltage of metal halide perovskite solar cells. Energy Environ Sci, 2016, 9: 3472–3481
86 Stranks SD, Burlakov VM, Leijtens T, *et al.* Recombination kinetics in organic-inorganic perovskites: Excitons, free charge, and subgap states. Phys Rev Appl, 2014, 2: 034007
87 Yamada Y, Nakamura T, Endo M, *et al.* Photocarrier recombination dynamics in perovskite $CH_3NH_3PbI_3$ for solar cell applications. J Am Chem Soc, 2014, 136: 11610–11613
88 Beattie AR, Landsberg PT. Auger effect in semiconductors. Proc R Soc Lond A, 1959, 249: 16–29
89 Haug A. Band-to-band Auger recombination in semiconductors. J Phys Chem Solids, 1988, 49: 599–605
90 Wright AD, Verdi C, Milot RL, *et al.* Electron-phonon coupling in hybrid lead halide perovskites. Nat Commun, 2016, 7: 11755
91 Price MB, Butkus J, Jellicoe TC, *et al.* Hot-carrier cooling and photoinduced refractive index changes in organic-inorganic lead halide perovskites. Nat Commun, 2015, 6: 8420
92 Deschler F, Price M, Pathak S, *et al.* High photoluminescence efficiency and optically pumped lasing in solution-processed mixed halide perovskite semiconductors. J Phys Chem Lett, 2014, 5: 1421–1426
93 Wehrenfennig C, Liu M, Snaith HJ, *et al.* Charge-carrier dynamics in vapour-deposited films of the organolead halide perovskite $CH_3NH_3PbI_{3-x}Cl_x$. Energy Environ Sci, 2014, 7: 2269–2275
94 Noel NK, Abate A, Stranks SD, *et al.* Enhanced photoluminescence and solar cell performance *via* Lewis base passivation of organic-inorganic lead halide perovskites. ACS Nano, 2014, 8: 9815–9821
95 Xing G, Mathews N, Sun S, *et al.* Long-range balanced electron- and hole-transport lengths in organic-inorganic $CH_3NH_3PbI_3$. Science, 2013, 342: 344–347
96 You J, Hong Z, Yang YM, *et al.* Low-temperature solution-processed perovskite solar cells with high efficiency and flexibility. ACS Nano, 2014, 8: 1674–1680
97 Liang PW, Liao CY, Chueh CC, *et al.* Additive enhanced crystallization of solution-processed perovskite for highly efficient planar-heterojunction solar cells. Adv Mater, 2014, 26: 3748–3754
98 Stranks SD, Eperon GE, Grancini G, *et al.* Electron-hole diffusion lengths exceeding 1 micrometer in an organometal trihalide perovskite absorber. Science, 2013, 342: 341–344
99 Shaw PE, Ruseckas A, Samuel IDW. Exciton diffusion measurements in poly(3-hexylthiophene). Adv Mater, 2008, 20: 3516–3520
100 Milot RL, Sutton RJ, Eperon GE, *et al.* Charge-carrier dynamics in 2D hybrid metal-halide perovskites. Nano Lett, 2016, 16: 7001–7007
101 Gonzalez-Pedro V, Juarez-Perez EJ, Arsyad WS, *et al.* General working principles of $CH_3NH_3PbX_3$ perovskite solar cells. Nano Lett, 2014, 14: 888–893
102 Zhao J, Kong G, Chen S, *et al.* Single crystalline $CH_3NH_3PbI_3$ self-grown on FTO/TiO_2 substrate for high efficiency perovskite solar cells. Sci Bull, 2017, 62: 1173–1176
103 Milot RL, Eperon GE, Snaith HJ, *et al.* Temperature-dependent charge-carrier dynamics in $CH_3NH_3PbI_3$ perovskite thin films. Adv Funct Mater, 2015, 25: 6218–6227
104 Yettapu GR, Talukdar D, Sarkar S, *et al.* Terahertz conductivity within colloidal $CsPbBr_3$ perovskite nanocrystals: Remarkably high carrier mobilities and large diffusion lengths. Nano Lett, 2016, 16: 4838–4848
105 Zhumekenov AA, Saidaminov MI, Haque MA, *et al.* Formamidinium lead halide perovskite crystals with unprecedented long carrier dynamics and diffusion length. ACS Energy Lett, 2016, 1: 32–37
106 Alarousu E, El-Zohry AM, Yin J, *et al.* Ultralong radiative states in hybrid perovskite crystals: Compositions for submillimeter diffusion lengths. J Phys Chem Lett, 2017, 8: 4386–4390
107 Wu B, Nguyen HT, Ku Z, *et al.* Discerning the surface and bulk recombination kinetics of organic-inorganic halide perovskite single crystals. Adv Energy Mater, 2016, 6: 1600551
108 Zhao D, Yu Y, Wang C, *et al.* Low-bandgap mixed tin-lead iodide perovskite absorbers with long carrier lifetimes for all-perovskite tandem solar cells. Nat Energy, 2017, 2: 17018
109 de Quilettes DW, Vorpahl SM, Stranks SD, *et al.* Impact of microstructure on local carrier lifetime in perovskite solar cells. Science, 2015, 348: 683–686
110 Wang JTW, Wang Z, Pathak S, *et al.* Efficient perovskite solar cells by metal ion doping. Energy Environ Sci, 2016, 9: 2892–2901
111 Zhang W, Pathak S, Sakai N, *et al.* Enhanced optoelectronic quality of perovskite thin films with hypophosphorous acid for planar heterojunction solar cells. Nat Commun, 2015, 6: 10030
112 Zuo L, Dong S, De Marco N, *et al.* Morphology evolution of high efficiency perovskite solar cells *via* vapor induced intermediate phases. J Am Chem Soc, 2016, 138: 15710–15716
113 Chen Q, Zhou H, Song TB, *et al.* Controllable self-induced passivation of hybrid lead iodide perovskites toward high performance solar cells. Nano Lett, 2014, 14: 4158–4163
114 Bu T, Liu X, Zhou Y, *et al.* A novel quadruple-cation absorber for universal hysteresis elimination for high efficiency and stable perovskite solar cells. Energy Environ Sci, 2017, 10: 2509–2515
115 Madjet ME, Berdiyorov GR, El-Mellouhi F, *et al.* Cation effect on hot carrier cooling in halide perovskite materials. J Phys Chem Lett, 2017, 8: 4439–4445
116 Lu H, Zhang H, Yuan S, *et al.* An optical dynamic study of $MAPbBr_3$ single crystals passivated with $MAPbCl_3/I_3$-$MAPbBr_3$ heterojunctions. Phys Chem Chem Phys, 2017, 19: 4516–4521
117 Ghosh D, Walsh Atkins P, Islam MS, *et al.* Good vibrations: Locking of octahedral tilting in mixed-cation iodide perovskites for solar cells. ACS Energy Lett, 2017, 2: 2424–2429
118 Roldán-Carmona C, Gratia P, Zimmermann I, *et al.* High efficiency methylammonium lead triiodide perovskite solar cells: The relevance of non-stoichiometric precursors. Energy Environ Sci, 2015, 8: 3550–3556
119 Turren-Cruz SH, Saliba M, Mayer MT, *et al.* Enhanced charge carrier mobility and lifetime suppress hysteresis and improve efficiency in planar perovskite solar cells. Energy Environ Sci, 2018, 11: 78–86
120 Abdi-Jalebi M, Andaji-Garmaroudi Z, Cacovich S, *et al.* Maximizing and stabilizing luminescence from halide perovskites with potassium passivation. Nature, 2018, 555: 497–501
121 Zhou Y, Yong ZJ, Zhang KC, *et al.* Ultrabroad photoluminescence and electroluminescence at new wavelengths from doped organometal halide perovskites. J Phys Chem Lett, 2016, 7: 2735–2741
122 Pérez-Del-Rey D, Forgács D, Hutter EM, *et al.* Strontium insertion in methylammonium lead iodide: Long charge carrier lifetime and high fill-factor solar cells. Adv Mater, 2016, 28: 9839–9845
123 Colella S, Mosconi E, Fedeli P, *et al.* $MAPbI_{3-x}Cl_x$ mixed halide perovskite for hybrid solar cells: The role of chloride as dopant on the transport and structural properties. Chem Mater, 2013, 25: 4613–4618
124 Kiermasch D, Rieder P, Tvingstedt K, *et al.* Improved charge carrier lifetime in planar perovskite solar cells by bromine doping. Sci Rep, 2016, 6: 39333
125 Ginting RT, Jung ES, Jeon MK, *et al.* Low-temperature operation of perovskite solar cells: With efficiency improvement and hysteresis-less. Nano Energy, 2016, 27: 569–576
126 Jiang Q, Zhao Y, Zhang X, *et al.* Surface passivation of perovskite film for efficient solar cells. Nat Photonics, 2019, 13: 460–466
127 Marchioro A, Teuscher J, Friedrich D, *et al.* Unravelling the mechanism of photoinduced charge transfer processes in lead iodide perovskite solar cells. Nat Photon, 2014, 8: 250–255
128 deQuilettes DW, Koch S, Burke S, *et al.* Photoluminescence lifetimes exceeding 8 μs and quantum yields exceeding 30% in hybrid perovskite thin films by ligand passivation. ACS Energy Lett, 2016, 1: 438–444
129 Brenes R, Guo D, Osherov A, *et al.* Metal halide perovskite polycrystalline films exhibiting properties of single crystals. Joule, 2017, 1: 155–167
130 Staub F, Rau U, Kirchartz T. Statistics of the Auger recombination of electrons and holes *via* defect levels in the band gap—application to lead-halide perovskites. ACS Omega, 2018, 3: 8009–8016
131 Song W, Cao G. Surface-defect passivation through complexation with organic molecules leads to enhanced power conversion efficiency and long term stability of perovskite photovoltaics. Sci China Mater, 2020, 63: 479–480
132 Zhou H, Chen Q, Li G, *et al.* Interface engineering of highly efficient

perovskite solar cells. Science, 2014, 345: 542–546
133 De Marco N, Zhou H, Chen Q, *et al.* Guanidinium: A route to enhanced carrier lifetime and open-circuit voltage in hybrid perovskite solar cells. Nano Lett, 2016, 16: 1009–1016
134 Lee JW, Kim HS, Park NG. Lewis acid-base adduct approach for high efficiency perovskite solar cells. Acc Chem Res, 2016, 49: 311–319
135 Lin Y, Shen L, Dai J, *et al.* π-conjugated Lewis base: Efficient trap-passivation and charge-extraction for hybrid perovskite solar cells. Adv Mater, 2017, 29: 1604545
136 Zheng X, Chen B, Dai J, *et al.* Defect passivation in hybrid perovskite solar cells using quaternary ammonium halide anions and cations. Nat Energy, 2017, 2: 17102
137 Zhao T, Chueh CC, Chen Q, *et al.* Defect passivation of organic-inorganic hybrid perovskites by diammonium iodide toward high-performance photovoltaic devices. ACS Energy Lett, 2016, 1: 757–763
138 de Quilettes DW, Zhang W, Burlakov VM, *et al.* Photo-induced halide redistribution in organic-inorganic perovskite films. Nat Commun, 2016, 7: 11683
139 Mosconi E, Meggiolaro D, Snaith HJ, *et al.* Light-induced annihilation of Frenkel defects in organo-lead halide perovskites. Energy Environ Sci, 2016, 9: 3180–3187
140 Tian Y, Peter M, Unger E, *et al.* Mechanistic insights into perovskite photoluminescence enhancement: Light curing with oxygen can boost yield thousandfold. Phys Chem Chem Phys, 2015, 17: 24978–24987
141 You J, Meng L, Song TB, *et al.* Improved air stability of perovskite solar cells *via* solution-processed metal oxide transport layers. Nat Nanotech, 2016, 11: 75–81
142 Heo JH, Han HJ, Kim D, *et al.* Hysteresis-less inverted $CH_3NH_3PbI_3$ planar perovskite hybrid solar cells with 18.1% power conversion efficiency. Energy Environ Sci, 2015, 8: 1602–1608
143 Zheng X, Wei Z, Chen H, *et al.* Designing nanobowl arrays of mesoporous TiO_2 as an alternative electron transporting layer for carbon cathode-based perovskite solar cells. Nanoscale, 2016, 8: 6393–6402
144 Liu X, Liu Z, Sun B, *et al.* 17.46% efficient and highly stable carbon-based planar perovskite solar cells employing Ni-doped rutile TiO_2 as electron transport layer. Nano Energy, 2018, 50: 201–211
145 Jiang Q, Zhang L, Wang H, *et al.* Enhanced electron extraction using SnO_2 for high-efficiency planar-structure $HC(NH_2)_2PbI_3$-based perovskite solar cells. Nat Energy, 2017, 2: 16177
146 Yang D, Yang R, Wang K, *et al.* High efficiency planar-type perovskite solar cells with negligible hysteresis using EDTA-complexed SnO_2. Nat Commun, 2018, 9: 3239
147 Biccari F, Gabelloni F, Burzi E, *et al.* Graphene-based electron transport layers in perovskite solar cells: A step-up for an efficient carrier collection. Adv Energy Mater, 2017, 7: 1701349
148 Huang C, Fu W, Li CZ, *et al.* Dopant-free hole-transporting material with a C_{3h} symmetrical truxene core for highly efficient perovskite solar cells. J Am Chem Soc, 2016, 138: 2528–2531
149 Yang L, Cai F, Yan Y, *et al.* Conjugated small molecule for efficient hole transport in high-performance p-i-n type perovskite solar cells. Adv Funct Mater, 2017, 27: 1702613
150 Kim GW, Kang G, Kim J, *et al.* Dopant-free polymeric hole transport materials for highly efficient and stable perovskite solar cells. Energy Environ Sci, 2016, 9: 2326–2333
151 Peng B, Yu G, Zhao Y, *et al.* Achieving ultrafast hole transfer at the monolayer MoS_2 and $CH_3NH_3PbI_3$ perovskite interface by defect engineering. ACS Nano, 2016, 10: 6383–6391
152 Tvingstedt K, Malinkiewicz O, Baumann A, *et al.* Radiative efficiency of lead iodide based perovskite solar cells. Sci Rep, 2014, 4: 6071
153 Yao J, Kirchartz T, Vezie MS, *et al.* Quantifying losses in open-circuit voltage in solution-processable solar cells. Phys Rev Appl, 2015, 4: 014020
154 Jensen N, Hausner RM, Bergmann RB, *et al.* Optimization and characterization of amorphous/crystalline silicon heterojunction solar cells. Prog Photovolt-Res Appl, 2002, 10: 1–13
155 Huang J, Yuan Y, Shao Y, *et al.* Understanding the physical properties of hybrid perovskites for photovoltaic applications. Nat Rev Mater, 2017, 2: 17042
156 Chen H, Ye F, Tang W, *et al.* A solvent- and vacuum-free route to large-area perovskite films for efficient solar modules. Nature, 2017, 550: 92–95
157 Yu W, Li F, Yu L, *et al.* Single crystal hybrid perovskite field-effect transistors. Nat Commun, 2018, 9: 5354
158 Kim YC, Kim KH, Son DY, *et al.* Printable organometallic perovskite enables large-area, low-dose X-ray imaging. Nature, 2017, 550: 87–91
159 Kang CH, Dursun I, Liu G, *et al.* High-speed colour-converting photodetector with all-inorganic $CsPbBr_3$ perovskite nanocrystals for ultraviolet light communication. Light Sci Appl, 2019, 8: 94
160 Xue J, Zhu Z, Xu X, *et al.* Narrowband perovskite photodetector-based image array for potential application in artificial vision. Nano Lett, 2018, 18: 7628–7634
161 Bao C, Zhu W, Yang J, *et al.* Highly flexible self-powered organolead trihalide perovskite photodetectors with gold nanowire networks as transparent electrodes. ACS Appl Mater Interfaces, 2016, 8: 23868–23875
162 Dou L, Yang YM, You J, *et al.* Solution-processed hybrid perovskite photodetectors with high detectivity. Nat Commun, 2014, 5: 5404
163 Fang Y, Huang J. Resolving weak light of sub-picowatt per square centimeter by hybrid perovskite photodetectors enabled by noise reduction. Adv Mater, 2015, 27: 2804–2810
164 Lin Q, Armin A, Lyons DM, *et al.* Low noise, IR-blind organohalide perovskite photodiodes for visible light detection and imaging. Adv Mater, 2015, 27: 2060–2064
165 Sutherland BR, Johnston AK, Ip AH, *et al.* Sensitive, fast, and stable perovskite photodetectors exploiting interface engineering. ACS Photonics, 2015, 2: 1117–1123
166 Tang F, Chen Q, Chen L, *et al.* Mixture interlayer for high performance organic-inorganic perovskite photodetectors. Appl Phys Lett, 2016, 109: 123301
167 Dong R, Fang Y, Chae J, *et al.* High-gain and low-driving-voltage photodetectors based on organolead triiodide perovskites. Adv Mater, 2015, 27: 1912–1918
168 Chen HW, Sakai N, Jena AK, *et al.* A switchable high-sensitivity photodetecting and photovoltaic device with perovskite absorber. J Phys Chem Lett, 2015, 6: 1773–1779
169 Saidaminov MI, Haque MA, Savoie M, *et al.* Perovskite photodetectors operating in both narrowband and broadband regimes. Adv Mater, 2016, 28: 8144–8149
170 Tan C, Tang M, Wu J, *et al.* Wafer-scale growth of single-crystal 2D semiconductor on perovskite oxides for high-performance transistors. Nano Lett, 2019, 19: 2148–2153
171 Zheng Z, Hu Q, Zhou H, *et al.* Submillimeter and lead-free $Cs_3Sb_2Br_9$ perovskite nanoflakes: Inverse temperature crystallization growth and application for ultrasensitive photodetectors. Nanoscale Horiz, 2019, 4: 1372–1379
172 Zhu H, Liu A, Luque HL, *et al.* Perovskite and conjugated polymer wrapped semiconducting carbon nanotube hybrid films for high-performance transistors and phototransistors. ACS Nano, 2019, 13: 3971–3981
173 Chen Y, Wu X, Chu Y, *et al.* Hybrid field-effect transistors and photodetectors based on organic semiconductor and $CsPbI_3$ perovskite nanorods bilayer structure. Nano-Micro Lett, 2018, 10: 57
174 Zou Y, Zou T, Zhao C, *et al.* A highly sensitive single crystal perovskite-graphene hybrid vertical photodetector. Small, 2020, 16: 2000733
175 Li S, Zhang Y, Yang W, *et al.* 2D perovskite $Sr_2Nb_3O_{10}$ for high-performance UV photodetectors. Adv Mater, 2020, 32: 1905443
176 Yakunin S, Sytnyk M, Kriegner D, *et al.* Detection of X-ray photons by solution-processed lead halide perovskites. Nat Photon, 2015, 9: 444–449
177 Jang HM, Kim JS, Heo JM, *et al.* Enhancing photoluminescence quantum efficiency of metal halide perovskites by examining luminescence-limiting factors. APL Mater, 2020, 8: 020904
178 Yuan M, Quan LN, Comin R, *et al.* Perovskite energy funnels for efficient light-emitting diodes. Nat Nanotech, 2016, 11: 872–877
179 Yang X, Zhang X, Deng J, *et al.* Efficient green light-emitting diodes based on quasi-two-dimensional composition and phase engineered perovskite with surface passivation. Nat Commun, 2018, 9: 570

180 Liang D, Peng Y, Fu Y, *et al.* Color-pure violet-light-emitting diodes based on layered lead halide perovskite nanoplates. ACS Nano, 2016, 10: 6897–6904
181 Zhang Q, Tavakoli MM, Gu L, *et al.* Efficient metal halide perovskite light-emitting diodes with significantly improved light extraction on nanophotonic substrates. Nat Commun, 2019, 10: 727
182 Li Z, Chen Z, Yang Y, *et al.* Modulation of recombination zone position for quasi-two-dimensional blue perovskite light-emitting diodes with efficiency exceeding 5%. Nat Commun, 2019, 10: 1027
183 Dulkeith E, Ringler M, Klar TA, *et al.* Gold nanoparticles quench fluorescence by phase induced radiative rate suppression. Nano Lett, 2005, 5: 585–589
184 Cho H, Jeong SH, Park MH, *et al.* Overcoming the electroluminescence efficiency limitations of perovskite light-emitting diodes. Science, 2015, 350: 1222–1225
185 Koscher BA, Swabeck JK, Bronstein ND, *et al.* Essentially trap-free $CsPbBr_3$ colloidal nanocrystals by postsynthetic thiocyanate surface treatment. J Am Chem Soc, 2017, 139: 6566–6569
186 Song J, Li J, Li X, *et al.* Quantum dot light-emitting diodes based on inorganic perovskite cesium lead halides ($CsPbX_3$). Adv Mater, 2015, 27: 7162–7167
187 Lin K, Xing J, Quan LN, *et al.* Perovskite light-emitting diodes with external quantum efficiency exceeding 20 per cent. Nature, 2018, 562: 245–248
188 Zhang Q, Su R, Du W, *et al.* Advances in small perovskite-based lasers. Small Methods, 2017, 1: 1700163
189 Liao Q, Hu K, Zhang H, *et al.* Perovskite microdisk microlasers self-assembled from solution. Adv Mater, 2015, 27: 3405–3410
190 Wang Z, Jingjing Q, Wang X, *et al.* Two-dimensional light-emitting materials: Preparation, properties and applications. Chem Soc Rev, 2018, 47: 6128–6174
191 Tsai H, Nie W, Blancon JC, *et al.* Stable light-emitting diodes using phase-pure Ruddlesden-Popper layered perovskites. Adv Mater, 2018, 30: 1704217
192 Byun J, Cho H, Wolf C, *et al.* Efficient visible quasi-2D perovskite light-emitting diodes. Adv Mater, 2016, 28: 7515–7520
193 Lanzetta L, Marin-Beloqui JM, Sanchez-Molina I, *et al.* Two-dimensional organic tin halide perovskites with tunable visible emission and their use in light-emitting devices. ACS Energy Lett, 2017, 2: 1662–1668
194 Sutter-Fella CM, Li Y, Amani M, *et al.* High photoluminescence quantum yield in band gap tunable bromide containing mixed halide perovskites. Nano Lett, 2016, 16: 800–806
195 Yang S, Niu W, Wang AL, *et al.* Ultrathin two-dimensional organic-inorganic hybrid perovskite nanosheets with bright, tunable photoluminescence and high stability. Angew Chem Int Ed, 2017, 56: 4252–4255
196 Lee S, Kim DB, Hamilton I, *et al.* Control of interface defects for efficient and stable quasi-2D perovskite light-emitting diodes using nickel oxide hole injection layer. Adv Sci, 2018, 5: 1801350
197 Matsushima T, Bencheikh F, Komino T, *et al.* High performance from extraordinarily thick organic light-emitting diodes. Nature, 2019, 572: 502–506
198 Zhang Y, Lim CK, Dai Z, *et al.* Photonics and optoelectronics using nano-structured hybrid perovskite media and their optical cavities. Phys Rep, 2019, 795: 1–51
199 Li S, Lei D, Ren W, *et al.* Water-resistant perovskite nanodots enable robust two-photon lasing in aqueous environment. Nat Commun, 2020, 11: 1192
200 Xu Y, Chen Q, Zhang C, *et al.* Two-photon-pumped perovskite semiconductor nanocrystal lasers. J Am Chem Soc, 2016, 138: 3761–3768
201 Zhang W, Peng L, Liu J, *et al.* Controlling the cavity structures of two-photon-pumped perovskite microlasers. Adv Mater, 2016, 28: 4040–4046
202 Liu W, Xing J, Zhao J, *et al.* Giant two-photon absorption and its saturation in 2D organic-inorganic perovskite. Adv Opt Mater, 2017, 5: 1601045
203 Zhu X, Xu H, Liu Y, *et al.* Two-photon up-conversion photoluminescence realized through spatially extended gap states in quasi-2D perovskite films. Adv Mater, 2019, 31: 1901240
204 Liu Z, Hu Z, Zhang Z, *et al.* Two-photon pumped amplified spontaneous emission and lasing from formamidinium lead bromine nanocrystals. ACS Photonics, 2019, 6: 3150–3158
205 Chen W, Bhaumik S, Veldhuis SA, *et al.* Giant five-photon absorption from multidimensional core-shell halide perovskite colloidal nanocrystals. Nat Commun, 2017, 8: 15198
206 Wu L, Chen K, Huang W, *et al.* Perovskite $CsPbX_3$: A promising nonlinear optical material and its applications for ambient all-optical switching with enhanced stability. Adv Opt Mater, 2018, 6: 1800400
207 Shao-he L, Jiu-sheng L. Terahertz modulator a using $CsPbBr_3$ perovskite quantum dots heterostructure. Appl Phys B, 2018, 124: 224
208 Lee KS, Kang R, Son B, *et al.* All-optical THz wave switching based on $CH_3NH_3PbI_3$ perovskites. Sci Rep, 2016, 6: 37912
209 Protesescu L, Yakunin S, Bodnarchuk MI, *et al.* Nanocrystals of cesium lead halide perovskites ($CsPbX_3$, X = Cl, Br, and I): Novel optoelectronic materials showing bright emission with wide color gamut. Nano Lett, 2015, 15: 3692–3696
210 Yang Z, Xu J, Zong S, *et al.* Lead halide perovskite nanocrystals-phospholipid micelles and their biological applications: Multiplex cellular imaging and *in vitro* tumor targeting. ACS Appl Mater Interfaces, 2019, 11: 47671–47679
211 Li P, Chen Y, Yang T, *et al.* Two-dimensional $CH_3NH_3PbI_3$ perovskite nanosheets for ultrafast pulsed fiber lasers. ACS Appl Mater Interfaces, 2017, 9: 12759–12765
212 Jiang G, Miao L, Yi J, *et al.* Ultrafast pulse generation from erbium-doped fiber laser modulated by hybrid organic-inorganic halide perovskites. Appl Phys Lett, 2017, 110: 161111
213 Bao X, Mu H, Chen Y, *et al.* Ytterbium-doped fiber laser passively mode locked by evanescent field interaction with $CH_3NH_3SnI_3$ perovskite saturable absorber. J Phys D-Appl Phys, 2018, 51: 375106
214 Miao L, Jiang G, Du L, *et al.* Erbium-doped fiber laser mode-locked by halide perovskite *via* evanescent field interaction. IEEE Photon Technol Lett, 2018, 30: 577–580
215 Hong S, Lédée F, Park J, *et al.* Mode-locking of all-fiber lasers operating at both anomalous and normal dispersion regimes in the C- and L-bands using thin film of 2D perovskite crystallites. Laser Photonics Rev, 2018, 12: 1800118
216 Meng L, You J, Yang Y. Addressing the stability issue of perovskite solar cells for commercial applications. Nat Commun, 2018, 9: 5265
217 Li N, Niu X, Chen Q, *et al.* Towards commercialization: The operational stability of perovskite solar cells. Chem Soc Rev, 2020, 49: 8235–8286
218 Berhe TA, Su WN, Chen CH, *et al.* Organometal halide perovskite solar cells: Degradation and stability. Energy Environ Sci, 2016, 9: 323–356
219 Bartel CJ, Sutton C, Goldsmith BR, *et al.* New tolerance factor to predict the stability of perovskite oxides and halides. Sci Adv, 2019, 5: eaav0693
220 Hieulle J, Wang X, Stecker C, *et al.* Unraveling the impact of halide mixing on perovskite stability. J Am Chem Soc, 2019, 141: 3515–3523
221 Jia C, Zhao X, Lai YH, *et al.* Highly flexible, robust, stable and high efficiency perovskite solar cells enabled by van der Waals epitaxy on mica substrate. Nano Energy, 2019, 60: 476–484
222 Asghar MI, Zhang J, Wang H, *et al.* Device stability of perovskite solar cells—A review. Renew Sustain Energy Rev, 2017, 77: 131–146

Acknowledgements This work was supported by the National Natural Science Foundation of China (51702219, 61975134, 61875138, 11772207 and 61961136001), the Science and Technology Innovation Commission of Shenzhen (KQJSCX20180328095501798, JCYJ20180507182047316, JCYJ20170811093453105, JCYJ20180307164612205, and GJHZ20180928160209731), the Natural Science Foundation of Hebei Province for distinguished young scholars (A2019210204), Guangdong Basic and Applied Basic Research Foundation (2020A1515110538), and China Postdoctoral Science Foundation (2021M692179).

Author contributions Zhao J and Zhang H provided the whole concept. Zhang F and Mi Z wrote the hole manuscript. Hao W drew the figures and checked the references. Cao G revised the manuscript. All authors contributed to the general discussions.

Conflict of interest The authors declare that they have no conflict of interest.

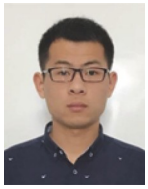

Feng Zhang is currently a postdoctoral researcher at the Collaborative Innovation Center for Optoelectronics and Technology, Shenzhen University. He received his bachelor's and master's degrees from Shandong Normal University in 2013 and 2017. Then, he achieved his PhD degree from Shenzhen University in 2020. His research interests focus on the nonlinear and ultrafast spectroscopies of low-dimensional materials and related devices.

Zhou Mi graduated from Hebei University of Science and Technology in 2019 with a bachelor's degree in inorganic non-metallic materials engineering. Since 2019, he has been studying for a master's degree at Shijiazhuang Tiedao University. His research direction is the preparation and performance of perovskite solar devices.

Han Zhang is currently the director of Shenzhen Key Laboratory of 2D Materials and Devices, and Shenzhen Engineering Laboratory of Phosphorene and Optoelectronics, Shenzhen University. He received his BSc degree from Wuhan University in 2006 and PhD degree from Nanyang Technological University in 2010. His current research focuses on ultrafast-, nonlinear-, and biophotonics of low-dimensional materials and devices.

Jinjin Zhao is the director of the Insititute of Materials for Energy Conversion, Shijiazhuang Tiedao University. She obtained her PhD degree in materials physics and chemistry from Shanghai Institute of Ceramics, Chinese Academy of Sciences (SICCAS) in 2010, under the supervision of Prof. Jianlin Shi and Prof. Hangrong Chen. She did her visiting doctoral studies at Max Plank Institute of Colloids and Interfaces, Germany, from October 2007 to October 2008, worked as a visiting scholar at the University of Washington from August 2015 to August 2016, and recently visited the City University of Hong Kong from July 2019 to October 2019. She held faculty appointment at Shijiazhuang Tiedao University. She is interested in probing instability mechanism in perovskite devices.

Guozhong Cao is Boeing-Steiner Professor of materials science and engineering and chemical engineering, and adjunct professor of mechanical engineering at the University of Washington (Seattle). His current research focuses on chemical processing of nanomaterials for energy-related applications including solar cells, rechargeable batteries, supercapacitors, and hydrogen storage. The research emphasis is to achieve novel structure and properties of energy-related nanostructured materials through processing and composition designing.

钙钛矿光电子器件中光致/电致载流子动力学调谐工程

张峰[1†], 秘周[2†], 郝伟仲[2], 陈华龙[1], 张俣乐[1], 赵晋津[2*], 曹国忠[3*], 张晗[1*]

摘要 过去十年以来, 具有非辐射复合损失低、载流子寿命和扩散长度长等优异特征的有机金属卤化物钙钛矿在光伏技术领域取得了长足进展. 有机金属卤化物钙钛矿具有卓越的光学性能和易于制备的特征, 其在电光和光电转换中得到广泛应用. 本文讨论了光激发自由载流子、激子的复合和扩散动力学特性. 这些动力学特性可以通过控制晶粒尺寸和晶界、抑制缺陷和界面电荷转移等多种方式进行控制. 并且讨论了在电光和光电转换器件中"有效载流子"的共性和差异. 在全光器件中, 强的光与物质相互作用会导致非线性效应, 如双光子吸收、自相位调制和光学漂白, 从而实现高分辨率成像、光调制和波长转换. 本综述为构建高性能光电器件提供了理论基础.

